Critical Role of Structural Order in Bipolar Redox-Active Molecules for Organic Redox Flow Batteries

Min Li, [†‖] Garvit Agarwal, [‡‖]Ilya A. Shkrob, [§‖] Ryan T. VanderLinden, [†] Julia Case, [†] Matt Prater, [†] Zayn Rhodes, [†‖] Rajeev S. Assary, [‡‖] Shelley D. Minteer [†‖*]

† Department of Chemistry, University of Utah, 315 South 1400 East, Salt Lake City, UT 84112, USA.

‡ Chemical Sciences and Engineering Division, Argonne National Laboratory, 9700 Cass Avenue, Argonne, IL 60439, USA.

§ Materials Science Division, Argonne National Laboratory, 9700 Cass Avenue, Argonne, IL 60439, USA.

‖ Joint Center for Energy Storage Research (JCESR), USA

Contents

I. Experimental and Computational Detail

1. Materials.

Organic solvents including acetonitrile (MeCN, 99.9+%, Extra Dry, AcroSeal), *N*,*N*-dimethylacetamide (DMA, 99.8%, Extra Dry, AcroSeal), and 1,2-dimethoxyethane (DME, 99%, Extra Dry, AcroSeal) were purchased from ACROS Organics (Fair Lawn, NJ). Tetraethylammonium bis(trifluoromethane)sulfonimide (TEATFSI, >98%) was obtained from IoLiTec GmbH (Heilbronn, Germany). Tetrabutylammonium hexafluorophosphate ($TBAPF_6$, ≥99.0%) was purchased from Sigma-Aldrich, Inc. (St. Louis, MO). *N*-(5-Bromoopentyl)phthalimide (97%), *N*-(3-Bromopropyl)phthalimide (98+%), *N*-(Bromomethyl)phthalimide (95%), phenothiazine (99%), sodium hydride (NaH, 60 wt% in mineral oil), 1,7-dibromoheptane (98%), and 1,9-dibromononane (97%), phthalimide potassium (98%)

were purchased from Fisher Scientific, Inc (Hampton, NH). All salts were dried in vacuum at 100 °C for two days before use. For electrochemical experiments, 0.5 M salts were dissolved in organic solvents in a glove box (O_2 < 0.5 ppm, H_2O < 0.5 ppm). To remove residual moisture, activated molecular sieves (3 Å) were added to the stock solutions for at least two days before use.

2. Synthesis

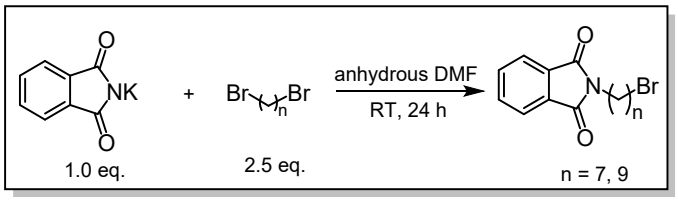

N-alkyl phthalimide bromide was synthesized based on the modified procedure from ref.[1]. As an example of the procedure, 1,7-dibromoheptane (0.097 mmol, 25 g) was dissolved in 100 mL of anhydrous *N*,*N*-dimethylformamide (DMF). Potassium phthalimide (0.039 mmol, 7.2 g) was then added to the reaction vessel, and the mixture was agitated using a magnetic stirrer for one day at 25 °C. The reaction product was then extracted by ethyl acetate (EtOAc) (3X), washed with water and brine, and dried over magnesium sulfate ($MgSO_4$). After removing most of the solvent in vacuum, the crude product was purified by flash column chromatography using hexane/EtOAc (9:1 v/v) as eluent. *N*-(9-bromonoyl)phthalimide was purified by gradient elution (0–5% EtOAc in hexanes).

N-(7-Bromoheptyl)phthalimide, clear liquid (11.3 g, 89.8% yield). ^{1}H NMR (500 MHz, $CDCl_3$) δ 7.88 – 7.79 (m, 2H), 7.74 – 7.66 (m, 2H), 3.67 (t, *J* = 7.3 Hz, 2H), 3.38 (t, *J* = 6.8 Hz, 2H), 1.84 (p, *J* = 6.9 Hz, 2H), 1.67 (q, *J* = 7.2 Hz, 2H), 1.42 (dq, *J* = 14.9, 6.1, 4.6 Hz, 2H), 1.38 – 1.31 (m, 4H).

N-(9-Bromonoyl)phthalimide, white cystalline solid (5.2 g, 82.9% yield). ^{1}H NMR (500 MHz, $CDCl_3$) δ 7.83 (dt, *J* = 7.4, 3.7 Hz, 2H), 7.70 (dd, *J* = 5.4, 3.1 Hz, 2H), 3.67 (t, *J* = 7.4 Hz, 2H), 3.39 (t, *J* = 6.9 Hz, 2H), 1.83 (p, *J* = 7.0 Hz, 2H), 1.66 (t, *J* = 7.2 Hz, 2H), 1.40 (t, *J* = 7.5 Hz, 2H), 1.31 (dt, *J* = 20.3, 4.6 Hz, 8H).

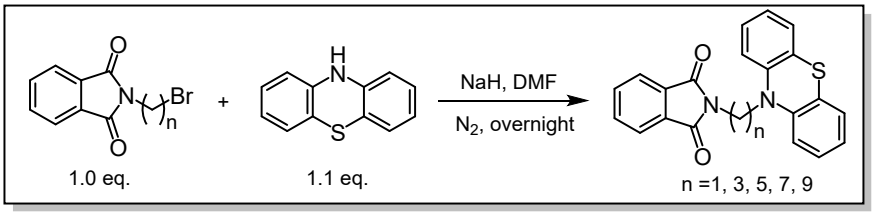

PPn (n= 1, 3, 5, 7, 9) molecules were synthesized by alkylation of phenothiazine with the suitable *N*-alkyl phthalimide bromide. As an example of the procedure, the sodium hydride (NaH, 60 wt% in mineral oil, 13.0 mol, 0.152g) was first introduced into a dry round bottom flask filled with the dry nitrogen. The flask was immersed into an ice bath, and oxygen-free solution of phenothiazine (11.0 mmol, 2.19 g) in anhydrous DMF (40 mL) was added dropwise to the NaH powder, and the reaction mixture was vigorously stirred for 30 min. Subsequently, an oxygen-free solution of *N*-(bromomethyl)phthalimide (10.0 mmol, 2.40g) in anhydrous DMF (40 mL) was cannular transferred to the mixture, and reacted under N_2 atmosphere overnight. The reaction was quenched with ice water, and the product was extracted with EtOAc (3X). The combined extractants were washed with water (5X) and brine, dried over $MgSO_4$, and the solvent was

removed in vacuum. The crude product was purified by flash column chromatography (gradient elution, 0–20% EtOAc in hexanes). The product was concentrated and dried in vacuum for 24 h at 80 °C.

PP1, chartreuse solid (2.5 g, 69.7% yield). ^{1}H NMR (500 MHz, $CDCl_3$) δ 7.82 – 7.77 (m, 2H), 7.70 – 7.65 (m, 2H), 7.22 – 7.14 (m, 4H), 7.14 – 7.08 (m, 2H), 6.97 (ddd, *J* = 7.7, 7.0, 1.6 Hz, 2H), 5.79 (s, 2H). ^{13}C NMR (126 MHz, $CDCl_3$) δ 167.55, 143.46, 134.12 (d, *J* = 6.1 Hz), 131.91, 127.53 (d, *J* = 5.3 Hz), 127.33 (d, *J* = 2.3 Hz), 123.82, 123.61, 118.19, 52.42.

PP3, white power (2.3 g, 59.5% yield). ^{1}H NMR (500 MHz, $CDCl_3$) δ 7.79 (dt, *J* = 7.8, 3.9 Hz, 2H), 7.68 (dd, *J* = 5.5, 3.1 Hz, 2H), 7.19 – 7.05 (m, 4H), 6.90 (t, *J* = 7.5 Hz, 2H), 6.84 (d, *J* = 8.1 Hz, 2H), 3.97 (t, *J* = 7.0 Hz, 2H), 3.83 (t, *J* = 7.0 Hz, 2H), 2.21 (p, *J* = 7.0 Hz, 2H). ^{13}C NMR (126 MHz, $CDCl3_3$) δ 168.24, 144.98, 133.86, 132.09, 127.49, 127.21, 125.62, 123.18, 122.61, 115.44, 44.96, 35.96, 26.26.

PP5, orange yellow solid (3.5 g, 84.4 % yield). ^{1}H NMR (500 MHz, $CDCl_3$) δ 7.86 – 7.79 (m, 2H), 7.71 (dd, *J* = 5.5, 3.0 Hz, 2H), 7.16 – 7.06 (m, 4H), 6.93 – 6.80 (m, 4H), 3.85 (t, *J* = 7.1 Hz, 2H), 3.67 (t, *J* = 7.1 Hz, 2H), 1.90 – 1.81 (m, 2H), 1.70 (ddd, *J* = 14.9, 7.9, 6.7 Hz, 2H), 1.53 – 1.43 (m, 2H). ^{13}C NMR (126 MHz, $CDCl_3$) δ 168.39, 145.20, 133.84, 132.17, 127.43, 127.19 (d, *J* = 2.5 Hz), 125.09, 123.17, 122.37, 115.40, 47.02, 37.77, 28.16, 26.38, 24.08.

PP7, bright yellow solid (2.1 g, 47.5 % yield). **^{1}H NMR** (500 MHz, THF-*d*8) δ 7.79 (dd, *J* = 5.3, 3.1 Hz, 2H), 7.72 (dd, *J* = 5.3, 3.1 Hz, 2H), 7.09 (td, *J* = 7.1, 1.5 Hz, 2H), 7.04 (dd, *J* = 7.6, 1.4 Hz, 2H), 6.91 (d, *J* = 8.1 Hz, 2H), 6.87 – 6.80 (m, 2H), 3.86 (t, *J* = 7.1 Hz, 2H), 3.59 (t, *J* = 7.2 Hz, 2H), 1.76 (p, *J* = 7.5 Hz, 2H), 1.61 (dddd, *J* = 7.4 Hz, 2H), 1.43 (dddd, *J* = 7.3, 6.8 Hz, 2H), 1.40 – 1.28 (m, 4H). **^{13}C NMR** (126 MHz, THF-*d*8) δ 169.36, 147.24, 135.41, 134.27, 128.77, 128.76, 126.81, 124.38, 123.81, 117.20, 48.71, 39.18, 30.57, 30.19, 28.53, 28.50, 28.46.

PP9, orange viscous liquid (4.3 g, 62.0 % yield). **^{1}H NMR** (500 MHz, THF-*d*8) δ 7.79 (dd, *J* = 5.3, 3.1 Hz, 2H), 7.72 (dd, *J* = 5.4, 3.0 Hz, 2H), 7.09 (td, *J* = 7.3, 1.4 Hz, 2H), 7.05 (dd, *J* = 7.6, 1.1 Hz, 2H), 6.90 (d, *J* = 8.1 Hz, 2H), 6.84 (td, *J* = 7.5, 1.1 Hz, 2H), 3.86 (t, *J* = 7.0 Hz, 2H), 3.59 (t, *J* = 7.2 Hz, 2H), 1.76 (dddd, *J* = 7.5 Hz, 2H), 1.61 (dddd, *J* = 7.3 Hz, 2H), 1.42 (dddd, *J* = 7.9 Hz, 2H), 1.35 – 1.22 (m, 8H). **^{13}C NMR** (126 MHz, THF-*d*8) δ 169.37, 147.25, 135.42, 134.27, 128.78, 128.76, 126.82, 124.38, 123.82, 117.21, 48.72, 39.23, 31.17, 30.88, 30.79, 30.27, 28.57, 28.53, 28.44.

3. Electronic Structure Calculations

All DFT calculations[2-3] for extended chain PPn molecules are carried out using Gaussian 16 software[4] and B3LYP/6-31+G(d,p) functional.[5] The solvation free energies are computed using SMD model[6] employing acetonitrile as the solvent medium. The geometries of PPn (n = 1-10) molecules were optimized in their neutral, oxidized, and reduced states. In addition to these calculations, we optimized geometries for gas-phase PP1 and cyclic PP5 (extracted from the crystal, see the section S7 for details) to assess the solvent effect on the charge transfer. The degree of charge transfer was estimated from the electrostatic charges (see the Zipped SI folder for details) in the redox active groups. To this end, we used the same approach that was used to compute partial atomic charges in our MD calculations (see section 8 below). The geometry optimized DFT structures were used to obtain CHelpG electrostatic charges in a single-point Hartree-Fock calculation. These charges where summed up for each redox moiety, giving the total charge on the heterocycle. The charge transfer can be characterized by the charge so defined shifted between the moieties when they are brought into contact. For larger molecules, such as PP5, this can be computed by comparing cyclic structures (in which there is a contact) and all-trans structures (in which the chain is extended and

there is no contact). For small molecules, the partial charges in the redox moieties were compared with all-extended PP9 molecule, in which the intramolecular charge was negligible. The purpose of SI is to provide inputs and topology files used for force field development for MD as opposed to the CT degree estimates. No such calculations are contained in these files, although the partial atomic charges given therein can be used for such estimates. The total charge on the heterocycles was compared with PP9 molecules, in which the intramolecular charge transfer was negligible.

The oxidation (E^{ox} vs. Li/Li$^+$) and reduction (E^{red} vs. Li/Li$^+$) potentials for PPn molecules were calculated using the change in Gibbs free energy in solution at 298 K upon removal ($\Delta G^{ox} = G^{oxidized} - G^{neutral}$) and addition ($\Delta G^{red} = G^{reduced} - G^{neutral}$) of an electron to a neutral molecule using eqs. S3.1 and S3.2, respectively.

$$E^{ox} = \frac{\triangle G^{ox}}{F} - 1.24\ \text{V} \qquad \text{(S3.1)}$$

$$E^{red} = \frac{-\triangle G^{red}}{F} - 1.24\ \text{V} \qquad \text{(S3.2)}$$

where F is the Faraday constant. The constant value of 1.24 V was subtracted to convert the change in Gibbs free energy to the reduction potential vs. Li/Li$^+$ reference electrode. More detail can be found in ref.[7]

Table S1. Highest occupied (HOMO) and lowest unoccupied (LUMO) molecular orbital isosurfaces of neutral PPn (n = 3,5,7) molecules.

BRMs	HOMO	LUMO
PP3	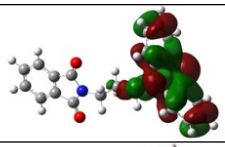	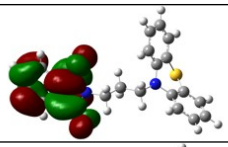
PP5	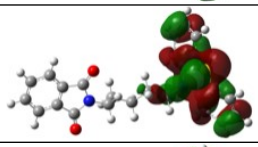	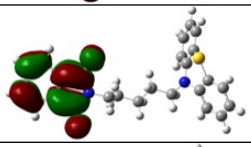
PP7	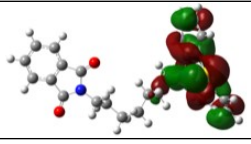	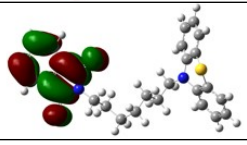

Table S2. Singly occupied molecular orbital (SOMO) of radical cations and LUMO isosurfaces of radical anions for PPn molecules (n= 1,3,5,7,9). Spin density maps for radical anions are also shown (the rightmost column). Below, α and b refer to the direction of the unpaired electron spin.

BRMs	α-SOMO	β-SOMO	α-LUMO	β-LUMO	Spin Density
PP1	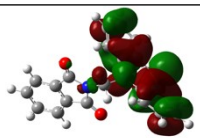	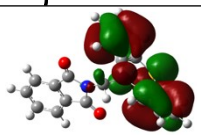	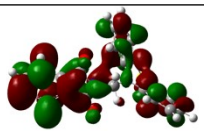	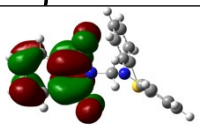	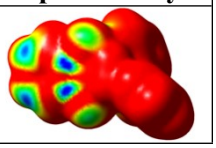

PP3	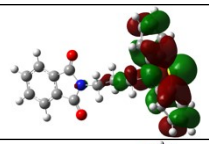	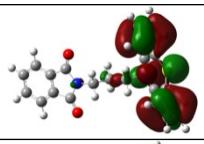	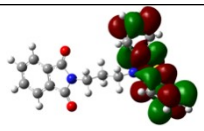	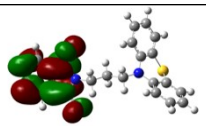	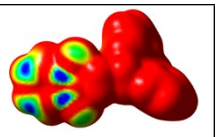
PP5	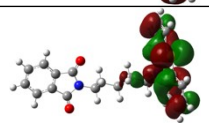	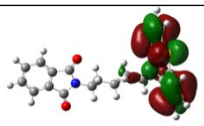	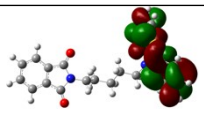	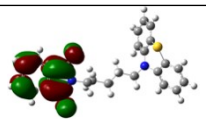	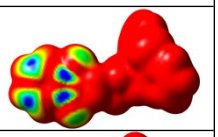
PP7	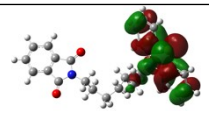	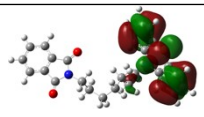	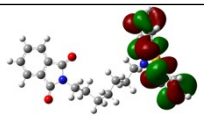	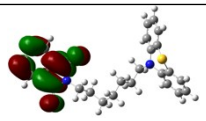	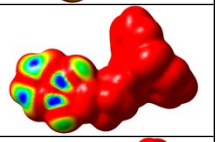
PP9	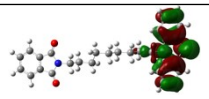	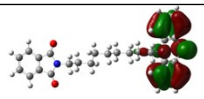	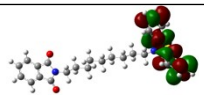	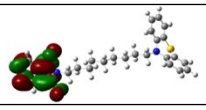	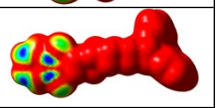

4. Cyclic voltammetry

All electrochemical experiments were conducted in an argon filled glovebox (O_2 < 0.5 ppm, H_2O < 0.5 ppm). Cyclic voltammetry (CV) was performed using standard three-electrode configuration with a 3 mm freshly polished glassy carbon electrode (Biologic VSP, France) as a working electrode, Ag/Ag^+ as a reference electrode (10 mM $AgNO_3$ in 0.5 M supporting electrolyte/organic solvent) (Bioanalytical Systems, Inc. West Lafayette, IN), and Pt wire mesh as a counter electrode. A low volume series cap kit (AF01CKT1004, Pine Research Instrumentation, Inc.) was used in these CV measurements. Ferrocene (3 mM solution) was used as an internal voltage reference.

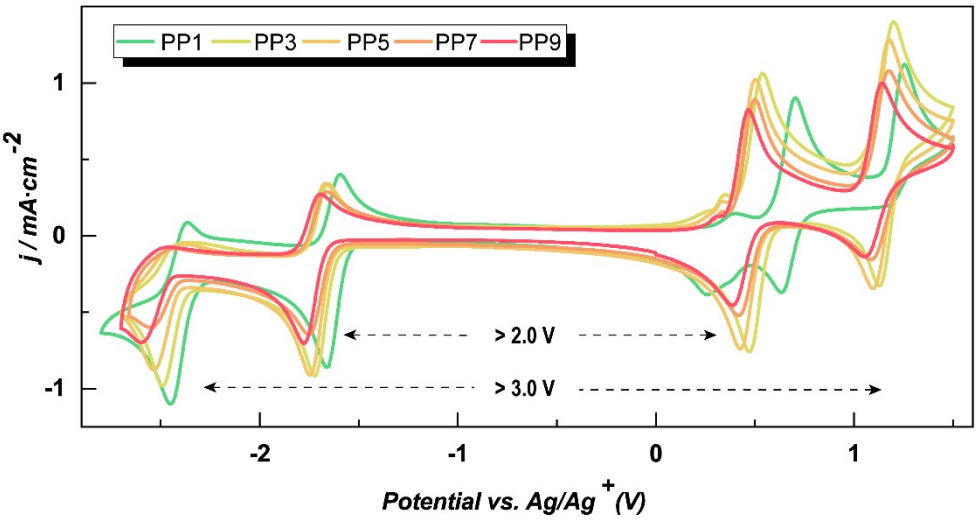

Figure S1. CVs for 3 mM PPn (n=1,3,5,7,9) in 0.5 M $TBAPF_6$/MeCN solutions at a scan rate of 0.1 V/s. The molecules are color coded as indicated at the top of the plot.

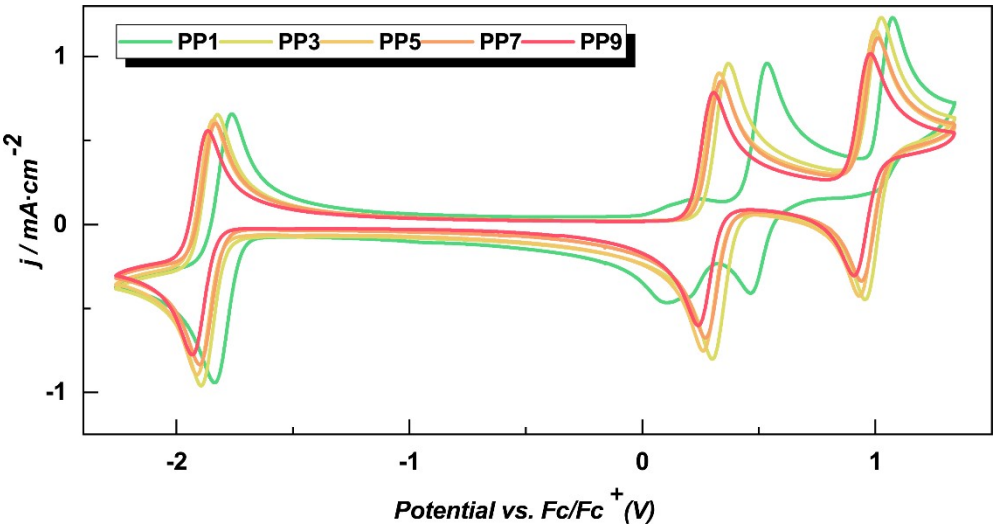

Figure S2. Reversibility of 2-electron oxidation of phenothiazine and 1-electron reduction of phthalimide in PPn molecules. The molecules are color coded as indicated at the top of the plot. The same conditions as in Figure S1.

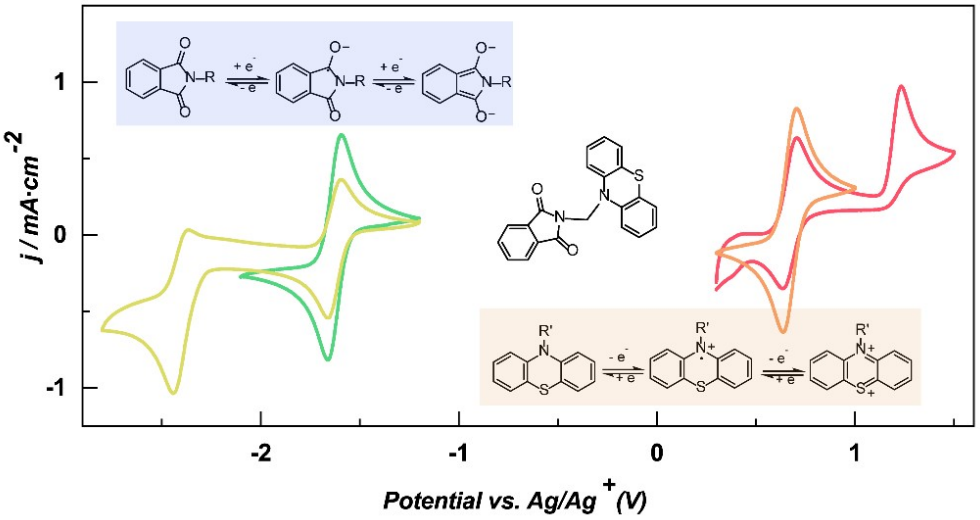

Figure S3. Evaluation of chemical reversibility for the donor and acceptor moieties in PP1 (shown in the inset). The same conditions as in Figure S1. The electrochemical reactions for phthalimide and phenothiazine are shown in the same plot.

5. Kinetic Studies

To evaluate kinetics, CVs at different scan rates v were obtained at 25 °C. Diffusion coefficients D of redox active bipolar molecules in different oxidation states (1-electron reactions only) were determined using the Randles-Sevick equation

$$i_p = 0.4463\, FAC^* \sqrt{\frac{FvD}{RT}}$$

where i_p is the peak redox current, F is the Faradays constant, R is the gas constant, T is the temperature. A is the active surface area of the electrode, C^* is the solute concentration, and v is the scanning rate (all in the SI units). The slope of the i_p vs. $v^{1/2}$ line yields the estimate for the diffusion coefficient.

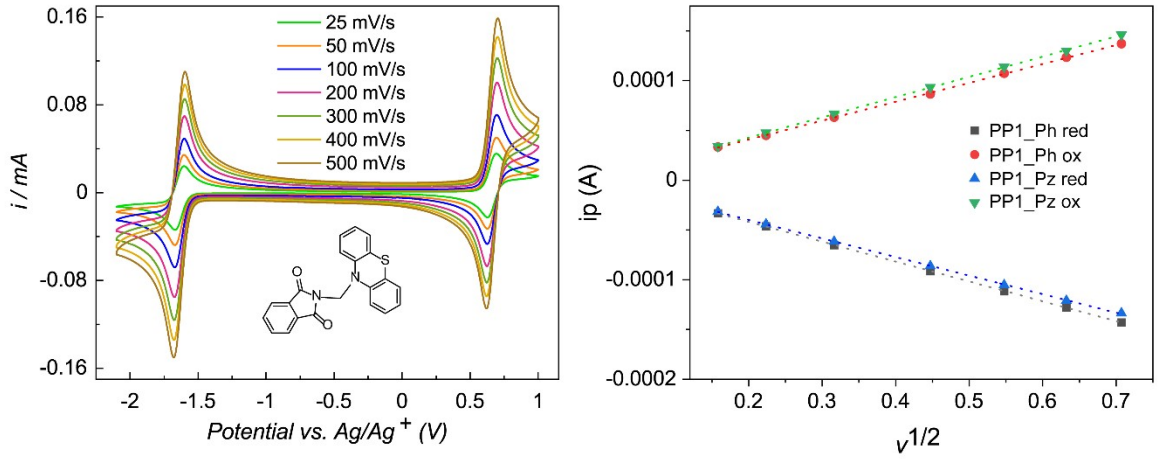

Figure S4. *On the left:* CVs obtained at various scan rates for PP1 in 0.5 M $TBAPF_6$/MeCN. *On the right:* The corresponding linear plots (eq. 1).

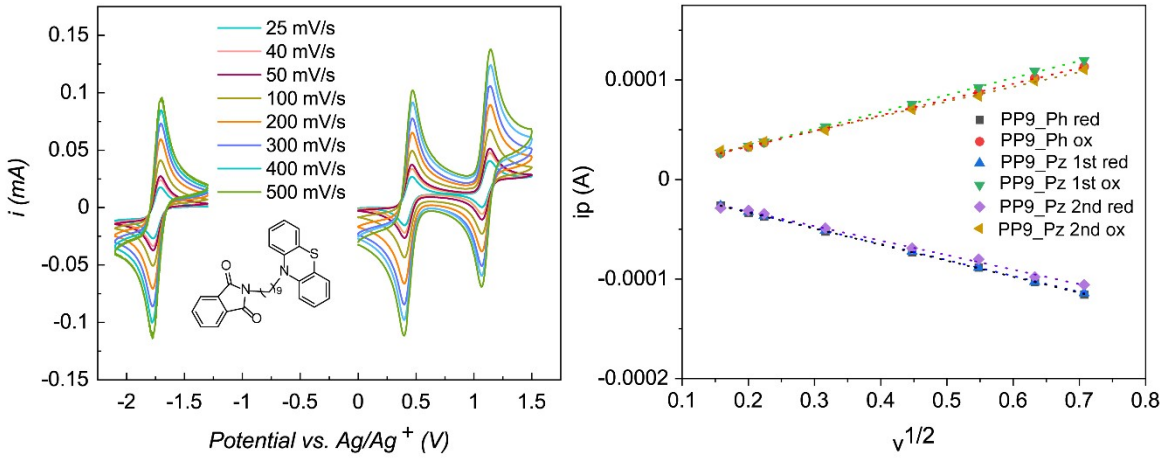

Figure S5. As Figure S4, for PP9.

Heterogeneous electron-transfer rate constants k^0 were determined using the Nicholson method.[8] Generally, the peak-to-peak separations (ΔE_p) depend on the dimensionless kinetic parameter Ψ defined in eq. S5.1, which is correlated to the charge transfer rate k^0 via eq. S5.2

$$\Psi = \frac{(-0.6288 + 0.0021\,\Delta E_p)}{1 - 0.017\,\Delta E_p} \qquad (S5.1)$$

$$\Psi = \frac{(D_o/D_R)^{\alpha/2} k^0}{(\pi D_o F v/RT)^{1/2}} \qquad (S5.2)$$

D_o and D_R refer to the diffusion coefficients of oxidative and reductive species, respectively. Plotting Ψ vs. $v^{1/2}$ gives the estimate of k^0 as shown in Figure S6. These kinetic data are summarized in Tables S5 to S8 below.

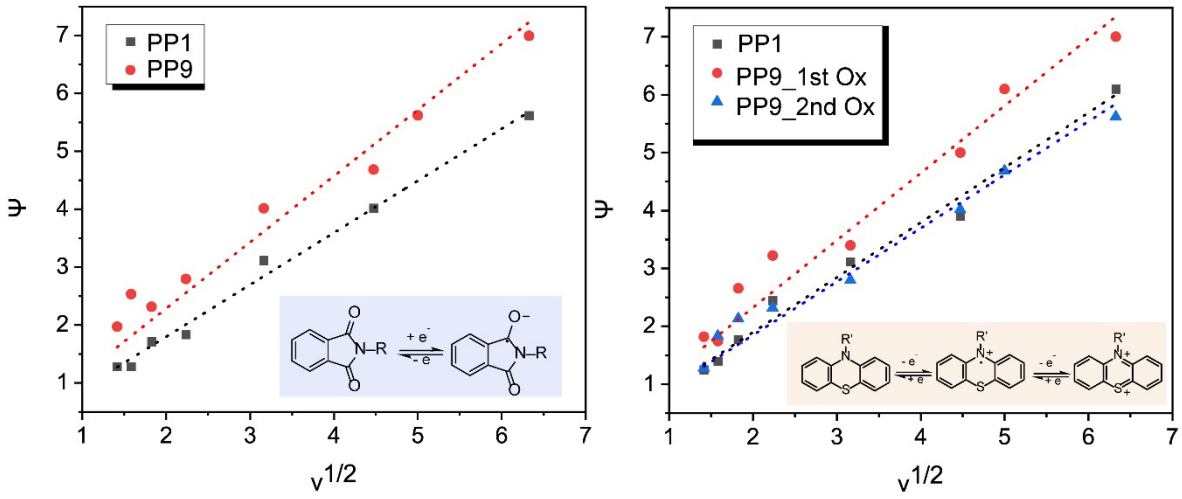

Figure S6. Representative plots of Ψ vs. $v^{1/2}$ for the reduction (*on the left*) and oxidation (*on the right*) of PP1 and PP9. See eqs. S5.1 and S5.2. The same experimental conditions as in Figure S1.

Table S3. Summary of kinetic parameters for 1-electron reactions of 3 mM PPn in 0.5 M $TBAPF_6$/MeCN (n=1,3,5,7,9).

	Phthalimide (acceptor)				Phenothiazine (donor)				
n	$E_{1/2}$ vs. Fc/Fc^+ (V)	$i_{p,ox}/i_{p,red}$	D ($cm^2\ s^{-1}$)	k^0 ($cm\ s^{-1}$)	$E_{1/2}$ vs. Fc/Fc^+ (V)	$i_{p,ox}/i_{p,red}$	D ($cm^2\ s^{-1}$)	k^0 ($cm\ s^{-1}$)	E_{cell} (V)
1	-1.80	0.97	1.22×10^{-5}	3.47×10^{-2}	0.50	1.08	1.22×10^{-5}	3.66×10^{-2}	2.30
3	-1.86	0.97	1.23×10^{-5}	3.55×10^{-2}	0.34	1.04	1.24×10^{-5}	3.61×10^{-2}	2.20
5	-1.88	0.98	1.08×10^{-5}	3.82×10^{-2}	0.30	1.04	1.18×10^{-5}	3.25×10^{-2}	2.17
7	-1.87	1.00	0.92×10^{-5}	3.05×10^{-2}	0.31	1.02	1.05×10^{-5}	3.00×10^{-2}	2.17
9	-1.90	0.99	0.81×10^{-5}	3.59×10^{-2}	0.27	1.04	0.91×10^{-5}	3.74×10^{-2}	2.17

Table S4. Kinetic parameters for the second oxidation of PPn (n=1,3,5,7,9). The same experimental conditions as in Table S4.

	Phenothiazine (second oxidation)				
n	$E_{1/2}$ vs. Fc/Fc^+ (V)	$i_{p,ox}/i_{p,red}$	D_o ($cm^2\ s^{-1}$)	k^0 ($cm\ s^{-1}$)	E_{cell} (V)
1	-	-	-	-	-
3	0.99	1.06	1.06×10^{-5}	3.68×10^{-2}	2.85
5	0.97	1.01	0.86×10^{-5}	2.87×10^{-2}	2.85
7	0.98	1.07	0.81×10^{-5}	3.04×10^{-2}	2.84
9	0.95	1.04	0.74×10^{-5}	2.77×10^{-2}	2.85

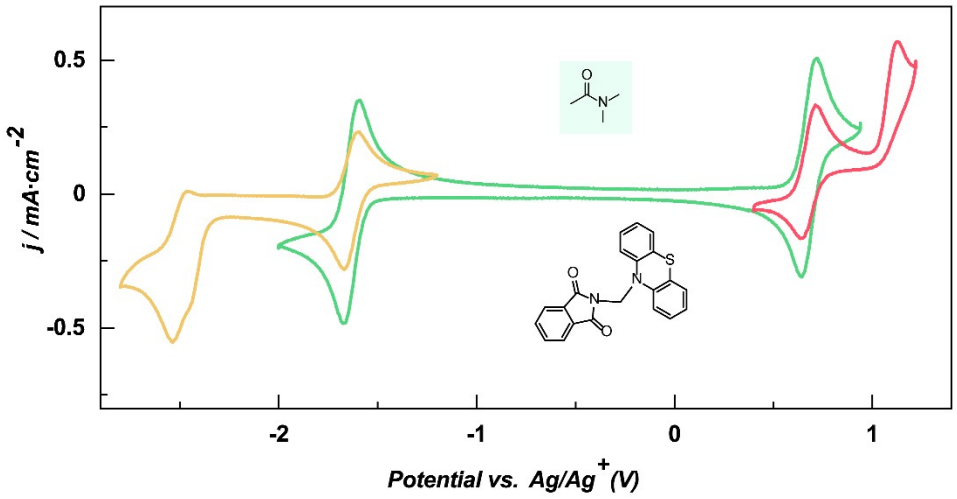

Figure S7. CVs of 3 mM PP1 in 0.5 M $TBAPF_6$/DMA (the structural formulas of the solvent molecule and PP1 are shown in the inset). PP3 and PP5 showed similar reversibility to PP1.

Table S5. Like Table S4, in DMA.

	Phthalimide (acceptor)				Phenothiazine (donor)				
n	$E_{1/2}$ vs. Ag/Ag^+ (V)	$i_{p,ox}/i_{p,red}$	D ($cm^2\ s^{-1}$)	k^0 ($cm\ s^{-1}$)	$E_{1/2}$ vs. Ag/Ag^+ (V)	$i_{p,ox}/i_{p,red}$	D ($cm^2\ s^{-1}$)	k^0 ($cm\ s^{-1}$)	E_{cell} (V)
1	-1.63	0.99	0.34×10^{-5}	1.46×10^{-2}	0.68	1.06	0.30×10^{-5}	1.32×10^{-2}	2.31
3	-1.68	0.99	0.39×10^{-5}	1.13×10^{-2}	0.52	1.04	0.34×10^{-5}	0.94×10^{-2}	2.20
5	-1.81	0.98	0.30×10^{-5}	0.98×10^{-2}	0.38	1.06	0.29×10^{-5}	1.40×10^{-2}	2.19

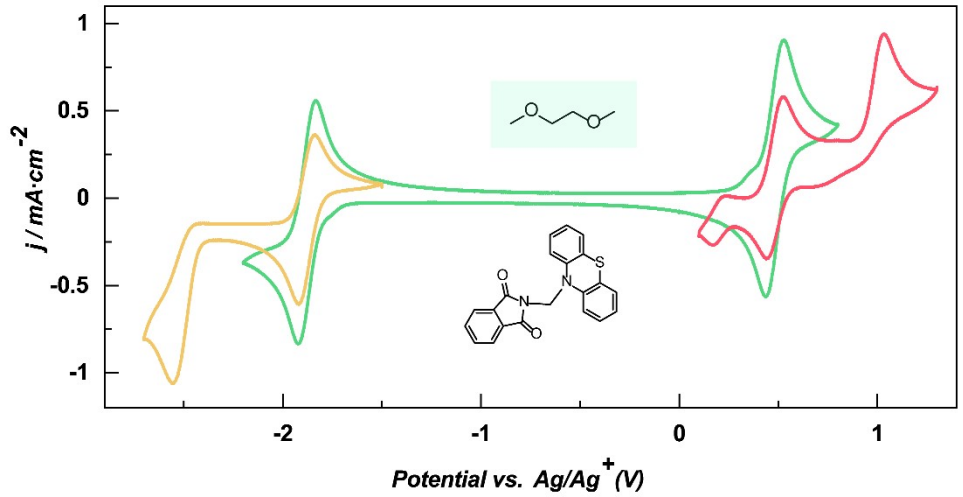

Figure S8. Like Figure S7, for DME solution of PP1.

Table S6. Like Table S5, in DME.

	Phthalimide (acceptor)				Phenothiazine (donor)				
n	$E_{1/2}$ vs. Ag/Ag^+ (V)	$i_{p,ox}/i_{p,red}$	D ($cm^2\ s^{-1}$)	k^0 ($cm\ s^{-1}$)	$E_{1/2}$ vs. Ag/Ag^+ (V)	$i_{p,ox}/i_{p,red}$	D ($cm^2\ s^{-1}$)	k^0 ($cm\ s^{-1}$)	E_{cell} (V)
1	-1.88	0.99	0.87×10^{-5}	0.97×10^{-2}	0.48	1.02	0.86×10^{-5}	0.96×10^{-2}	2.36
3	-1.94	1.00	0.78×10^{-5}	1.06×10^{-2}	0.34	1.03	0.79×10^{-5}	1.09×10^{-2}	2.27
5	-1.97	0.98	0.75×10^{-5}	0.55×10^{-2}	0.30	1.02	0.77×10^{-5}	0.57×10^{-2}	2.27

6. Solubility Measurements

The solubility of PPn (n = 1, 3, 5, 7, 9) was evaluated spectophotometrically using a Thermo Scientific Evolution 260 Bio UV-Visible Spectrophotometer. Liquid solutions of the known composition (< 0.2 mM) were transferred into a 1 cm optical path quartz glass cuvette (Starna Cells), and the optical densities were determined. The absorbance around 300 nm was used to obtain calibration plots shown in Figures S9 to S11. To prepare saturated solutions at 25 °C, the redox-active material was added in small portions to a vigorously stirred electrolyte, until it could not be dissolved. To ensure that the solutions reached equilibrium, the mixtures settled overnight. Subsequently, supernatant was removed and diluted to the range of calibration curves. For each solubility measurement, three dilutions were used to estimate the standard deviation.

The optical absorption spectra of PP1 in MeCN, DMA, and DME solutions are shown on the right side in Figure S9-S11, respectively. In these spectra, the absorbance peak at ~ 300 nm is from the phenothiazine group,[9] while the peaks observed at shorter wavelengths are from the phthalimide.[10] The ratios between the intensities of these absorption bands change with the solvent, reflecting the effect of solvent polarity on the extent of D-A charge transfer. Figure S12 summarizes the effect of the salt on the solubility of PPn in acetonitrile.

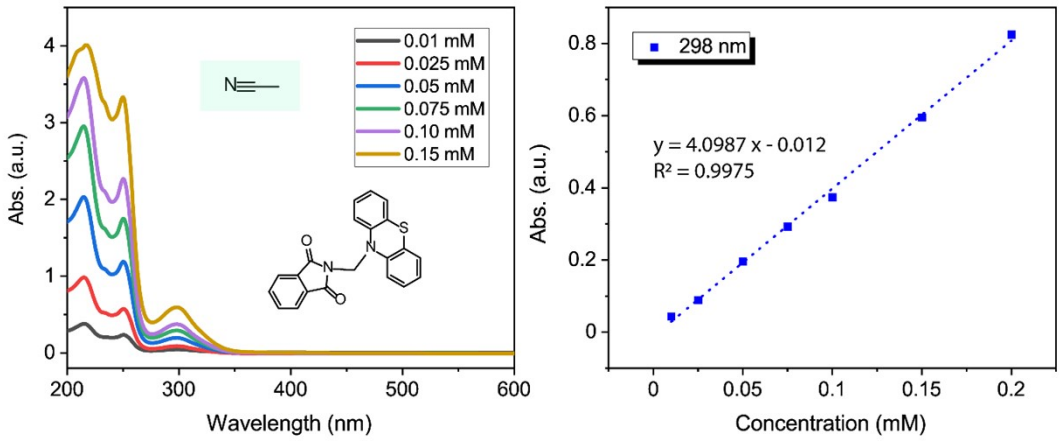

Figure S9. Representative UV-vis spectra of PP1 in MeCN. The peaks at 300 nm are from the phenothiazine group, while the two peaks at shorter wavelengths are from the phthalimide group.

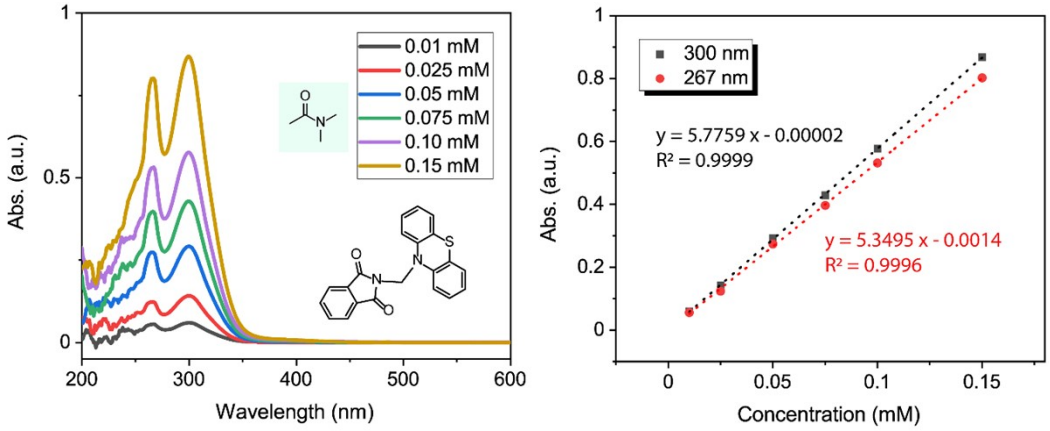

Figure S10. Like Figure S9, for DMA. In the concentration plot, the optical densities absorption peaks at 267 and 300 nm are plotted together.

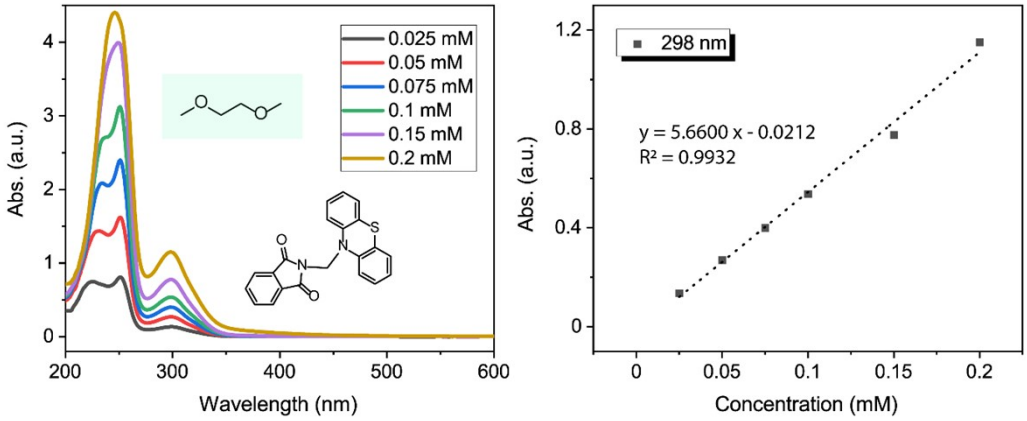

Figure S11. Like Figure S9, for DME.

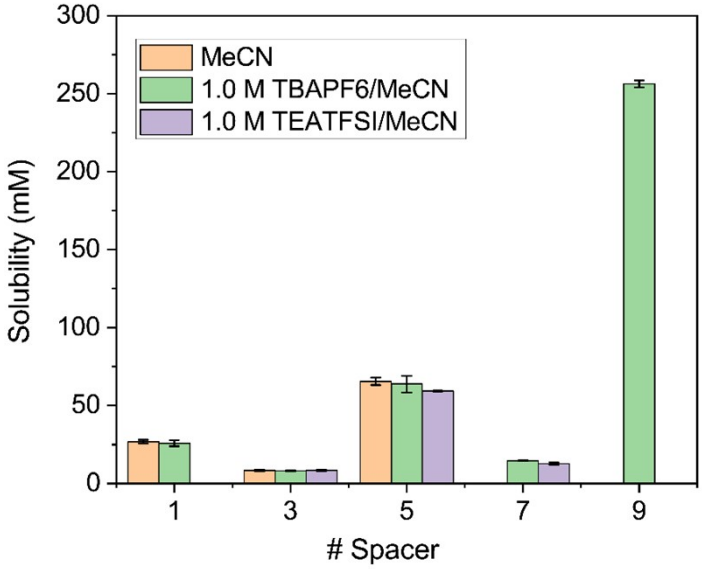

Figure S12. Evaluation of the effect of supporting electrolyte on the solubility in MeCN.

7. Crystal Structure Determination

Single-crystal X-ray diffraction data was collected using a Nonius Kappa CCD diffractometer equipped with and a BRUKER APEXII CCD detector and Mo Kα radiation (λ = 0.71073 Å). The APEX3[11] software suite was used to manage data collection, integration (SAINT), absorption correction by the Multi-scan method (SADABS),[12] structure determination via direct methods (SHLEXT), and and model refinement (SHELXL)[13] using established refinement strategies.[14] All X-ray data was collected at 100 K. All non-hydrogen atoms were refined anisotropically. The positions of hydrogen atoms were calculated geometrically and refined using a riding model. All crystal structures have been deposited with the Cambridge Crystallographic Data Centre (CCDC). The CIF and PDB formatted structures are given in the zipped SI folder. Table S7 summarizes crystallographic data for four PPn molecules.

Table S7. The summary of crystallographic data for PPn molecules.

Property	**PP1**	**PP3**	**PP5**	**PP7**	**PP9**
CCDC entry	2071533	2071534	2071535	2071536	2072890
space group	P 2_1/n	P b c a	P b c a	P 2_1/c	P 2_1/n
Z	4	8	8	8	4
a, Å	5.305	11.072	8.625	22.734	5.109
b, Å	17.335	8.413	16.095	21.760	28.160
c, Å	17.810	38.997	29.008	8.947	17.072
α, °	90	90	90	90	90
β, °	90.429	90	90	99.528	98.418
γ, °	90	90	90	90	90
unit cell volume, Å^3	1637.66	3632.51	4026.89	4364.76	2429.79
molecular volume, Å^3	409.42	454.06	503.36	545.60	607.45
density, g/cm^3	1.454	1.413	1.367	1.347	1.286
R-factor, %	4.38	3.57	4.26	4.52	4.56
C=O(A)…H(D), Å [a]	2.373		2.488		
C=O(A)…H(D), Å [b]	2.652	2.308	2.511	2.547	
A-A π-stacking [c]	no	no	yes	yes	no
Chain-crossed pairs	no	yes	no	yes	no

a) the shortest distance between the carbonyl oxygen in phthalimide and ring hydrogen in phenothiazine moieties (intramolecular), b) ditto, intermolecular, c) 3.7 Å antiparralel stacks.

The crystal structures were further "refined" using PM7 semiempirical method[15] in MOPAC suite[16] to compute partial electrostatic charges on the molecules in the crystal. During this refinement, the space group was retained but the unit cell parameters and molecular geometries were optimized. The refined cells and electrostatic charges are contained in the zipped SI folder.

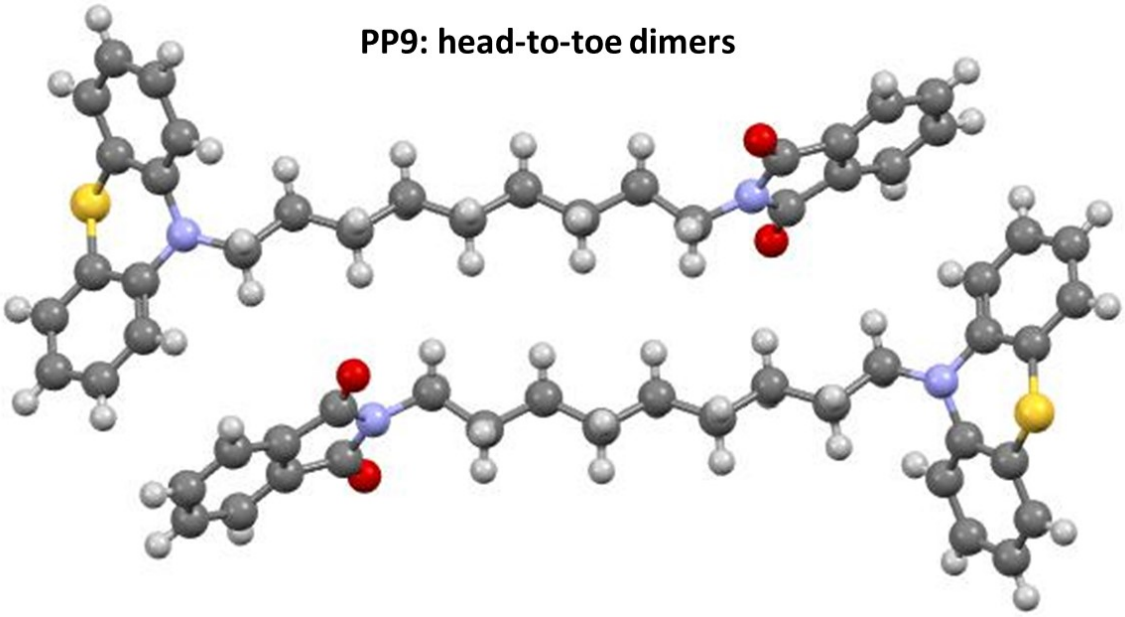

Figure S13. Head-to-toe, side-by-side extended-chain PP9 pairs observed in PP9 crystals.

8. Molecular Dynamics (MD) Simulations

Nonpolarized OPLS-AA force field[17-18] in a LibParGen implementation[19-20] was used for the bond, angle, and torsion potentials in PPn molecules. The partial atomic charges were calculated using CHelpG method[21-22] in a single-point Hartree-Fock calculation with the DFT optimized geometry (see Section 4 above). The input topology files for all PPn molecules (n=1-9) are given in the zipped SI folder along with representative MD frames in the Protein Data Bank (PDB) format. NPT equilibration at 1 bar at 300 K (2 ns) was used to estimate the density using the Parrinello-Rahman barostat with the solution compressibility of 9.5×10^{-5} bar^{-1}. Particle mesh Ewald summation was used to account for electrostatic interactions, and the modified Berendsen thermostat was used to rescale atomic velocities. Short-range cutoffs of 1.1 nm were implemented, and the interatomic van der Waals interactions were parameterized using the OPLS-AA force field.[17-18] For NVT equilibration, we ran the MD trajectory for 2 ns at 300 K and then sampled it over 4 ns to obtain 200 equally spaced time frames. The initial configuration was generated using Packmol[23], and the MD trajectories were computed using Gromacs 2018.[24] The VMD package[25] was used for visualization of the MD snapshots. The input topologies for the three solvents (MeCN, DMA, and DME) are also contained in the zipped SI folder.

Note that the classical MD model does not include polarization and did not explicitly treat charge transfer between the donor and acceptor moieties for bipolar molecules in solution. In some simulations, we artificially moved 0.1 e- between the ring hydrogen atoms in the donor and the carbonyl oxygen atoms in the acceptor. While this ad hoc "charge transfer" changed clustering metrics, it did not change the qualitative trends. The concentration of 0.14 M corresponded to 1080 DME and 16 PPn molecules in a ~5.7 nm box. This concentration was used to look at clustering in DME solutions as it traverses the extremes of solubility as determined experimentally.

Graph theory methods were used to analyze the clustering/connectivity networks using iGraph package.[26] Each PPn molecule was represented by a node in an undirected graph; two molecules making a contact gave the graph edge. The coordination number (CN) is defined as the average degree of the node (the number of molecular contacts). The overall graph connectivity is characterized by the global and mean

local connectivity clustering coefficient C_2. This coefficient gives the probability of the three nodes making a triangle if two of them make a wedge.[27] These coefficients can be counted globally for the entire graph or locally for each node and then averaged.

Another way to characterize the connectivity is by computing the eigenvalues and eigenvectors of the adjacency matrix, in which 1 corresponds to an edge between the nodes (i.e., the two molecules contacting each other) and 0 is for no connection. The need to involve such less intuitive quantities is a wide distribution of the node degrees (i.e., the contacts coordination numbers) in the graphs: the spectral graph theory can give estimates of connectivity taking this spread into account. The largest eigenvalue (λ_{max}), which is also called the spectral radius of the graph, characterizes the extent of connectivity and the inverse participation ratio (IPR) for the corresponding eigenvalue v_q (defined as $\left(\sum_q v_q^4\right)^{-1}$) characterizes the spread of the connected cluster over the graph.[28] These metrics are averaged over the MD trajectory. Table S4 gives the computed parameters some of which are also shown in Figures 9a and 9b in the main text. The neighborhood statistics N*x* indicate the average percentage of molecules in contact with the *x* like molecules.

Table S8. Neighborhood statistics and clustering parameters for PPn molecules in 0.14 M solution in DME (1 bar, 300 K), from MD simulations.

n	N0 [a]	N1	N2	N3	Spectral Radius [b]	Mean IPR [c]	Mean CN [d]	mean local C2 [e]	global C2 [f]
PP1	60.07	25.47	13.71	0.65	1.644	2.8	0.552	0.0827	0.3477
PP2	54.48	29.23	14.55	1.74	1.81	2.97	0.636	0.1144	0.4952
PP3	40.98	36.88	19.99	2.05	1.79	3.1	0.834	0.1149	0.3454
PP4	32.46	34.24	29.04	4.14	2.035	3.41	1.052	0.1787	0.4413
PP5	57.59	28.61	11.94	1.87	1.634	2.93	0.581	0.0464	0.1743
PP6	35.67	33.21	21.8	7.71	2.257	3.86	1.064	0.1409	0.3607
PP7	41.14	43.19	12.9	2.64	1.637	3.11	0.774	0.0383	0.1183
PP8	52.55	38.68	7.9	0.81	1.416	2.7	0.572	0.0253	0.0997
PP9	47.23	35.91	12.03	4.1	1.809	3.45	0.752	0.0407	0.1317

a) Nx are the percentage of molecules with exactly x neighbors by the atom-atom proximity criterion r<2.8 Å, b) the maximum eigenvalue of the adjacency matrix, c) the mean inverse participation ratio for PPn clusters, d) the mean coordination ratio for the clusters, e,f) the mean local and global clustering coefficients (the probability of finding three contacting molecules if two pairs of the molecules are contacting).

9. Bulk Electrolysis

Bulk electrolysis of PPn molecules was performed in a static, symmetric H-cell equipped with reticulated vitreous carbon electrodes (100 ppi, Duocell). A porous glass frit (P5, Adams and Chittenden) was used as a separator. On the working side of the H-cell, an $Ag/AgNO_3$ electrode (10 mM $AgNO_3$ in 0.5 M

$TBAPF_6$/MeCN) was used as a reference. Both chambers initially contained 5 mM PPn solutions in 0.5 M $TBAPF_6$/MeCN and were stirred continuously during electrochemical cycling. Before electrolysis, electrochemical impedance spectroscopy was used to ensure similar resistivity for different active materials. In the plots below, CE and EE stand for the coulombic and energy efficiencies, respectively. The active materials were initially charged to 100% state-of-charge (0.67 mAh). See the main text for other details.

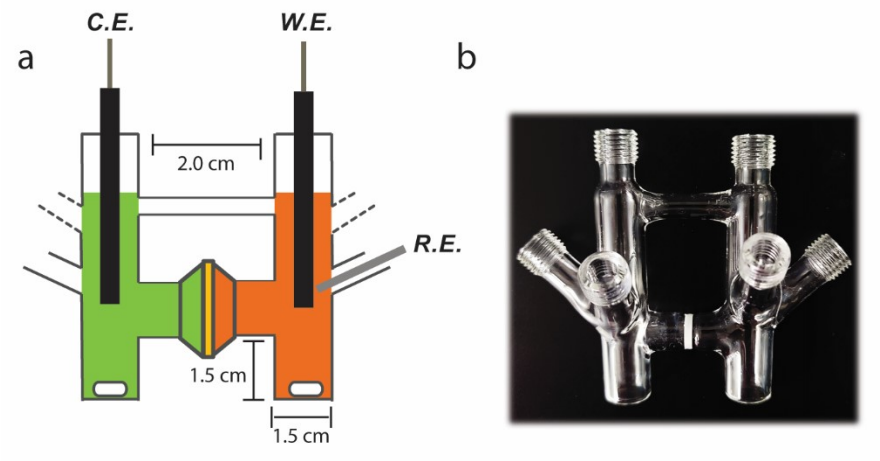

Figure S14. **(a)** Schematic illustration of the custom H-cells. **(b)** Photograph of the bulk electrolysis cell.

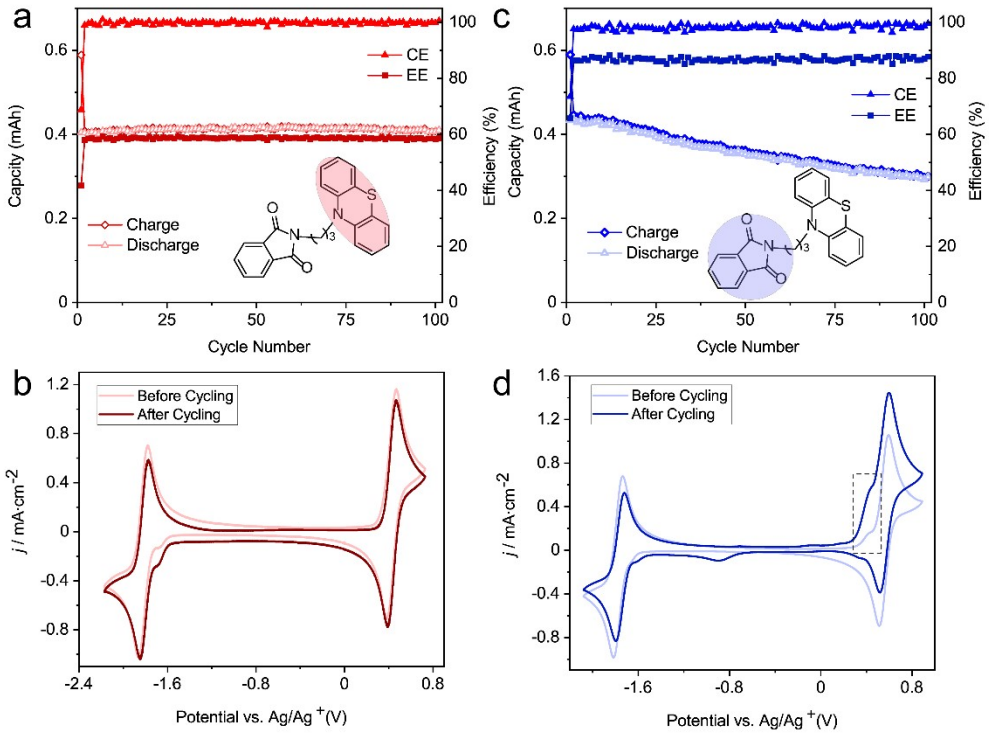

Figure S15. Cycling performance of the phenothiazine donor (**a,b**) and phthalimide acceptor (**c,d**) over 100 charge/discharge cycles at 5 mA. (**b,d**) CV analysis of PP3 before and after cycling of the donor and acceptor, respectively.

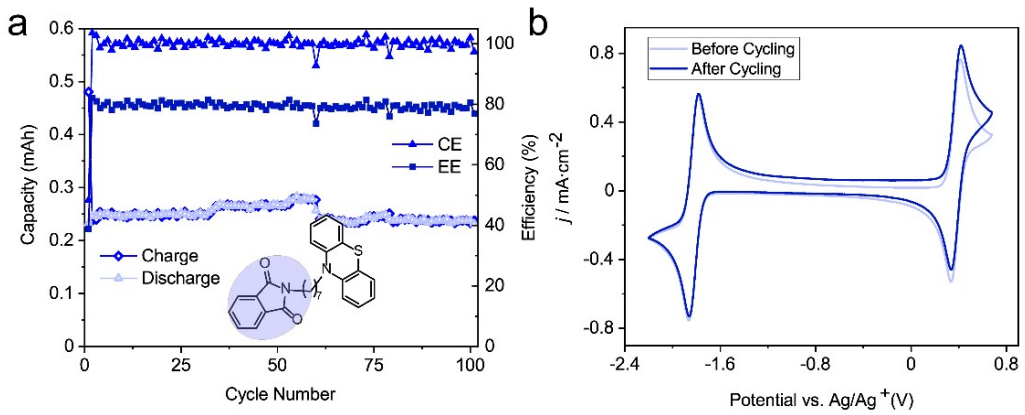

Figure S16. Cycling performance of the phthalimide acceptor in 5 mM PP7 in 0.5 M $TBAPF_6$/DMA. **(a)** cell capacity, CE, and EE performance over 100 charge/discharge cycles at 5 mA. **(b)** CV analysis before and after cycling of the acceptor in PP7.

II. NMR Spectra

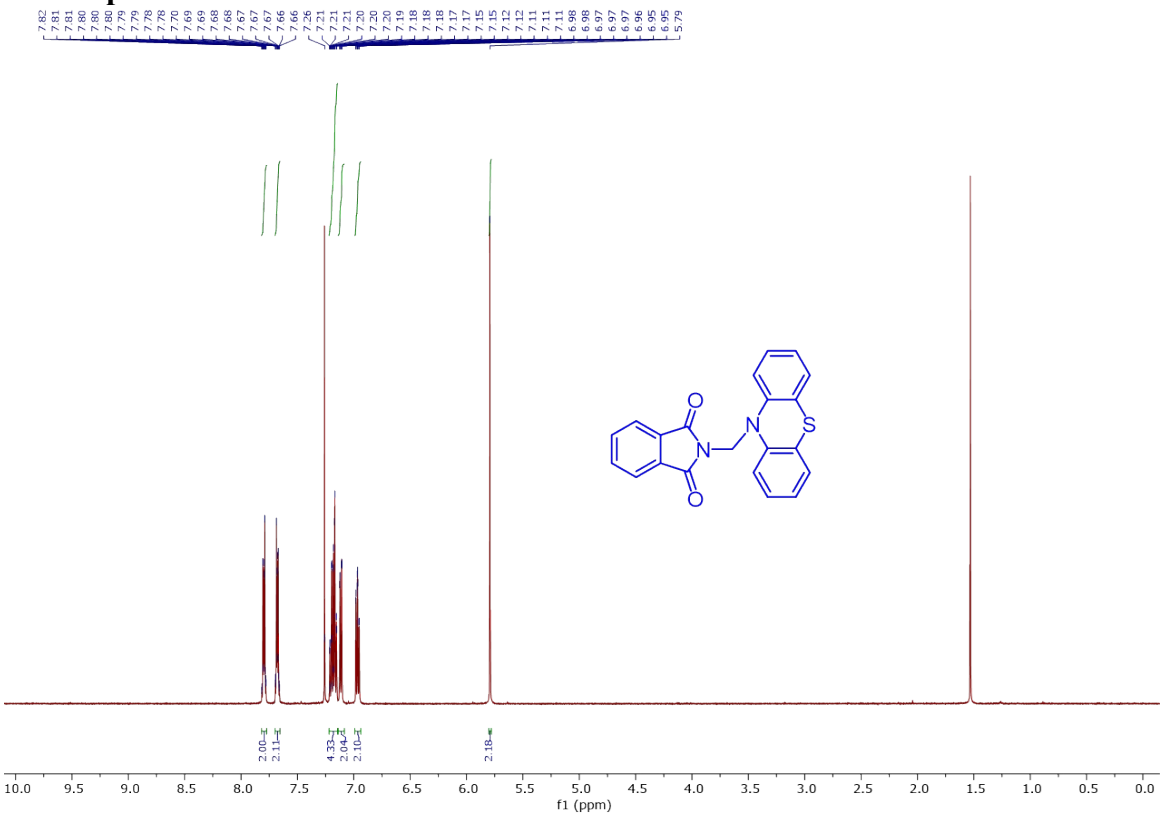

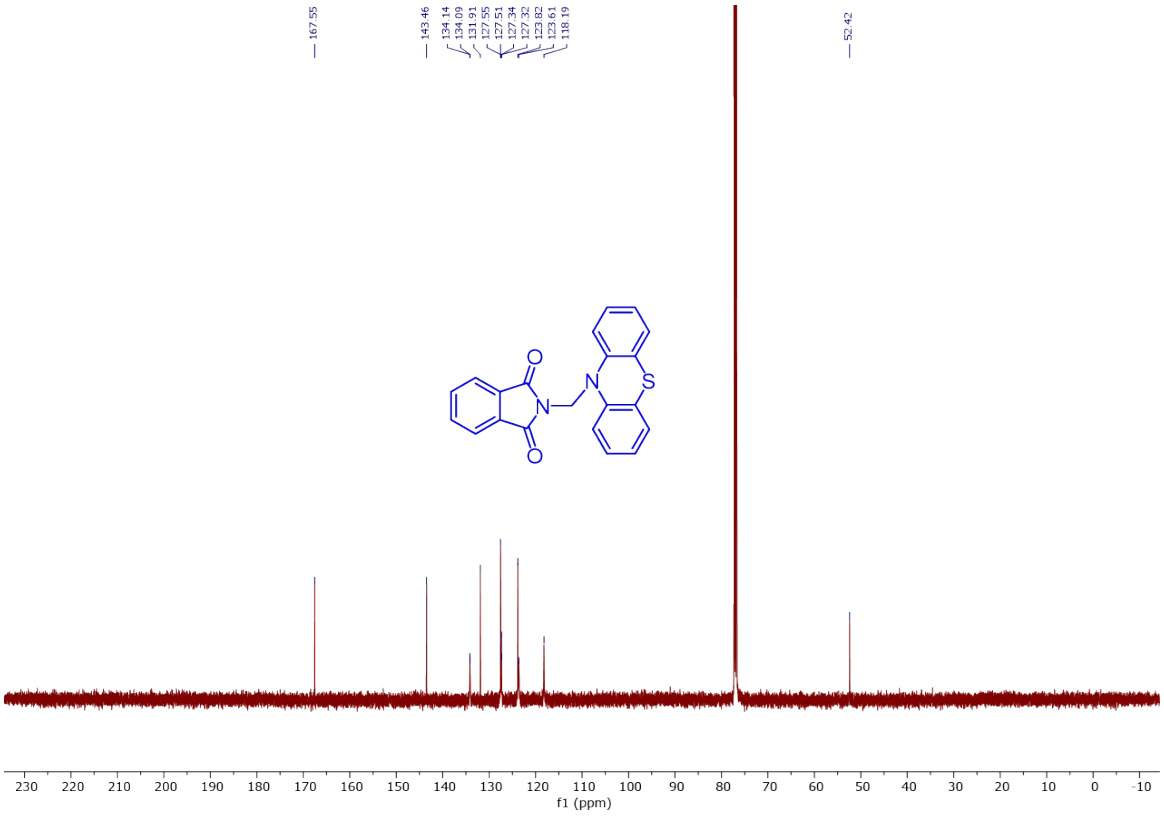
167.55
143.46
134.14
134.09
131.91
127.55
127.51
127.34
127.32
123.82
123.61
118.19
52.42
f1 (ppm)

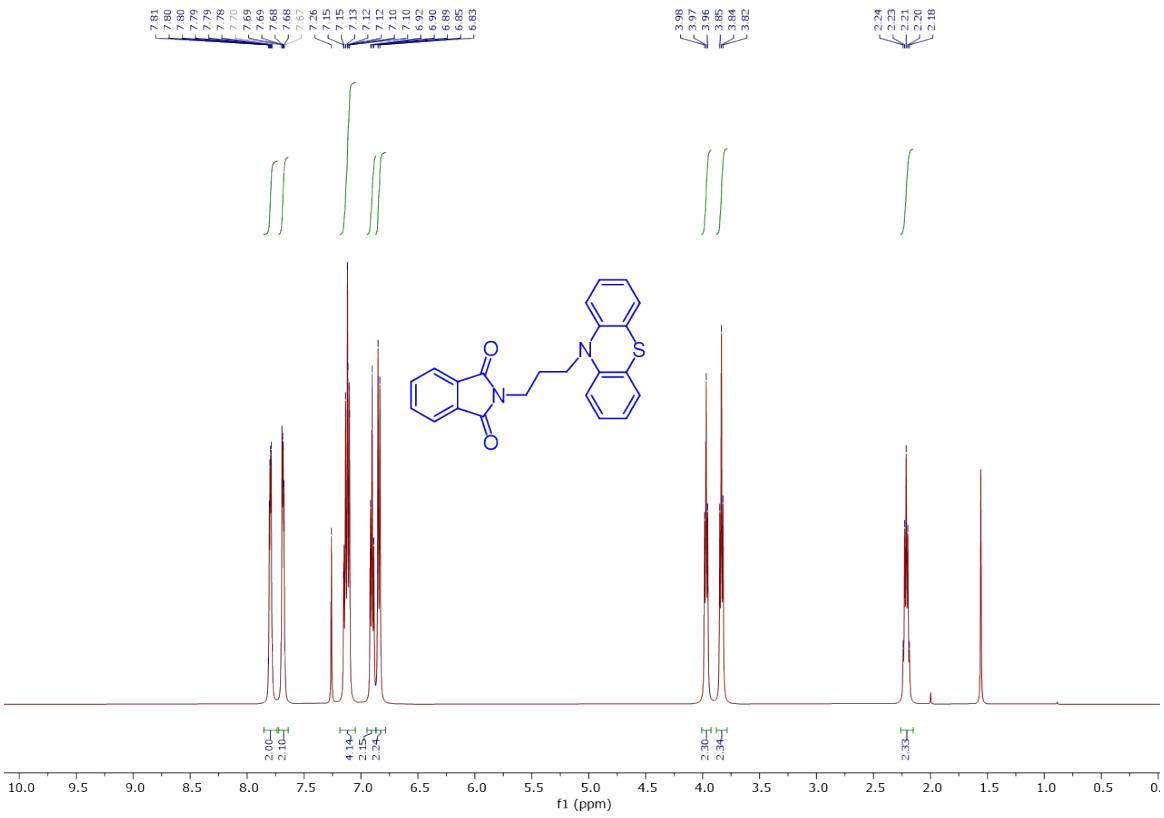
7.81
7.80
7.80
7.79
7.79
7.78
7.70
7.69
7.69
7.68
7.68
7.67
7.26
7.15
7.15
7.13
7.12
7.12
7.10
7.10
6.92
6.90
6.89
6.85
6.83
3.98
3.97
3.96
3.85
3.84
3.82
2.24
2.23
2.21
2.20
2.18
2.00
2.10
4.14
2.15
2.24
2.30
2.34
2.33
f1 (ppm)

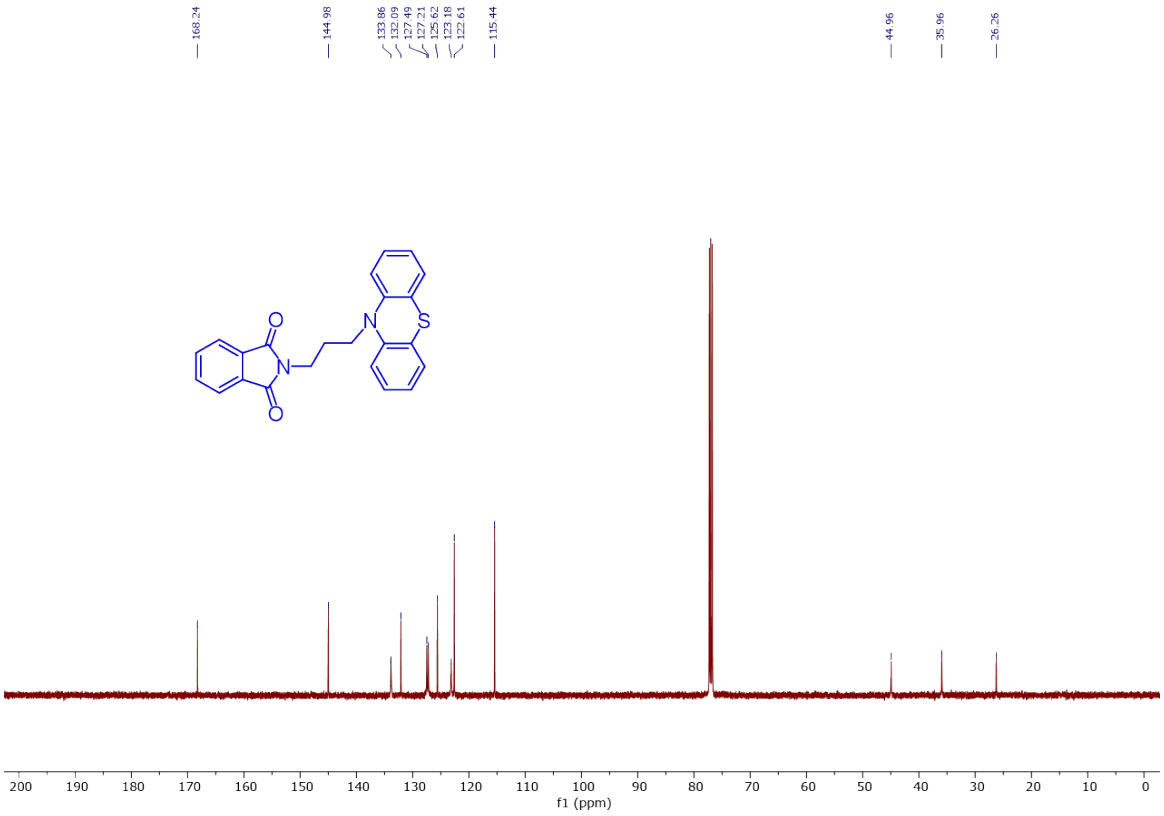
168.24
144.98
133.86
132.09
127.49
127.21
125.62
123.18
122.61
115.44
44.96
35.96
26.26
f1 (ppm)

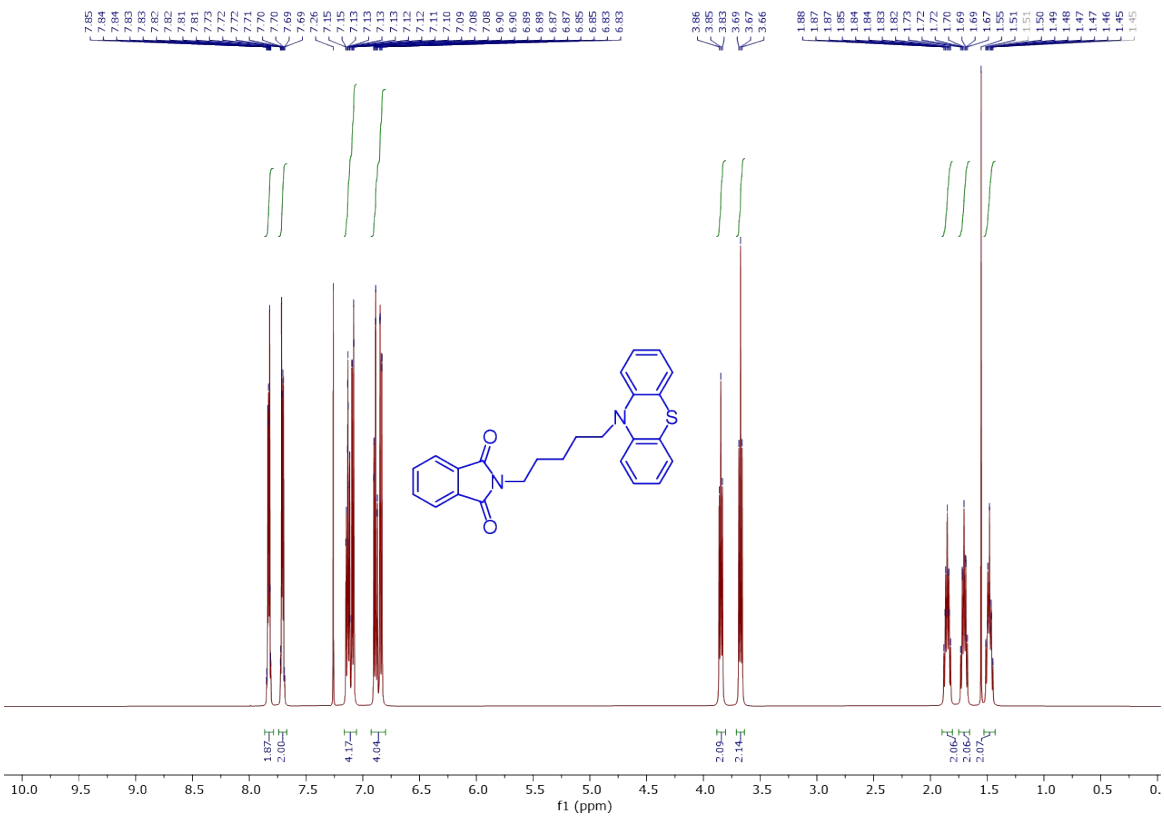
f1 (ppm)

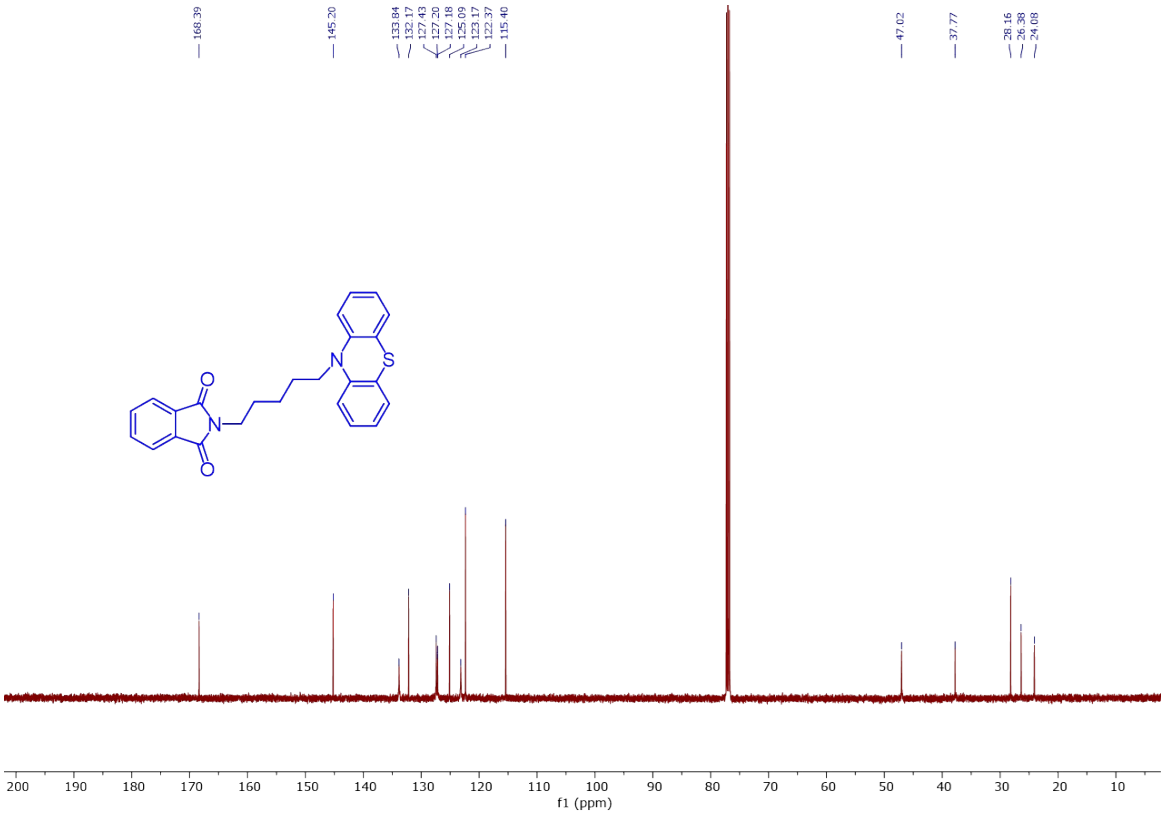
168.39
145.20
133.84
132.17
127.43
127.20
127.18
125.09
123.17
122.37
115.40
47.02
37.77
28.16
26.38
24.08
N
S
O
O
f1 (ppm)

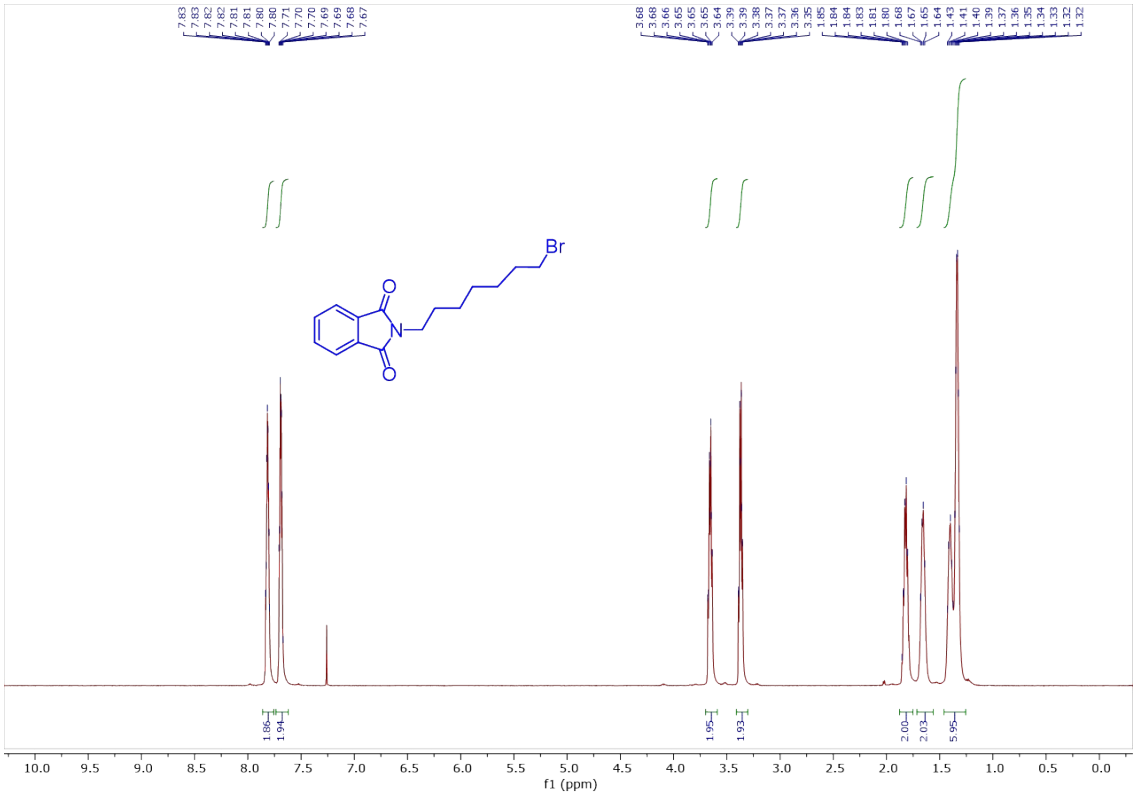
7.83
7.83
7.82
7.82
7.81
7.81
7.80
7.80
7.71
7.70
7.70
7.69
7.69
7.68
7.67
3.68
3.68
3.66
3.65
3.65
3.64
3.39
3.38
3.38
3.37
3.37
3.36
3.35
1.85
1.84
1.84
1.83
1.81
1.80
1.68
1.67
1.65
1.64
1.43
1.41
1.40
1.39
1.37
1.36
1.35
1.34
1.33
1.32
1.32
Br
O
O
N
1.86
1.94
1.95
1.93
2.00
2.03
5.95
f1 (ppm)

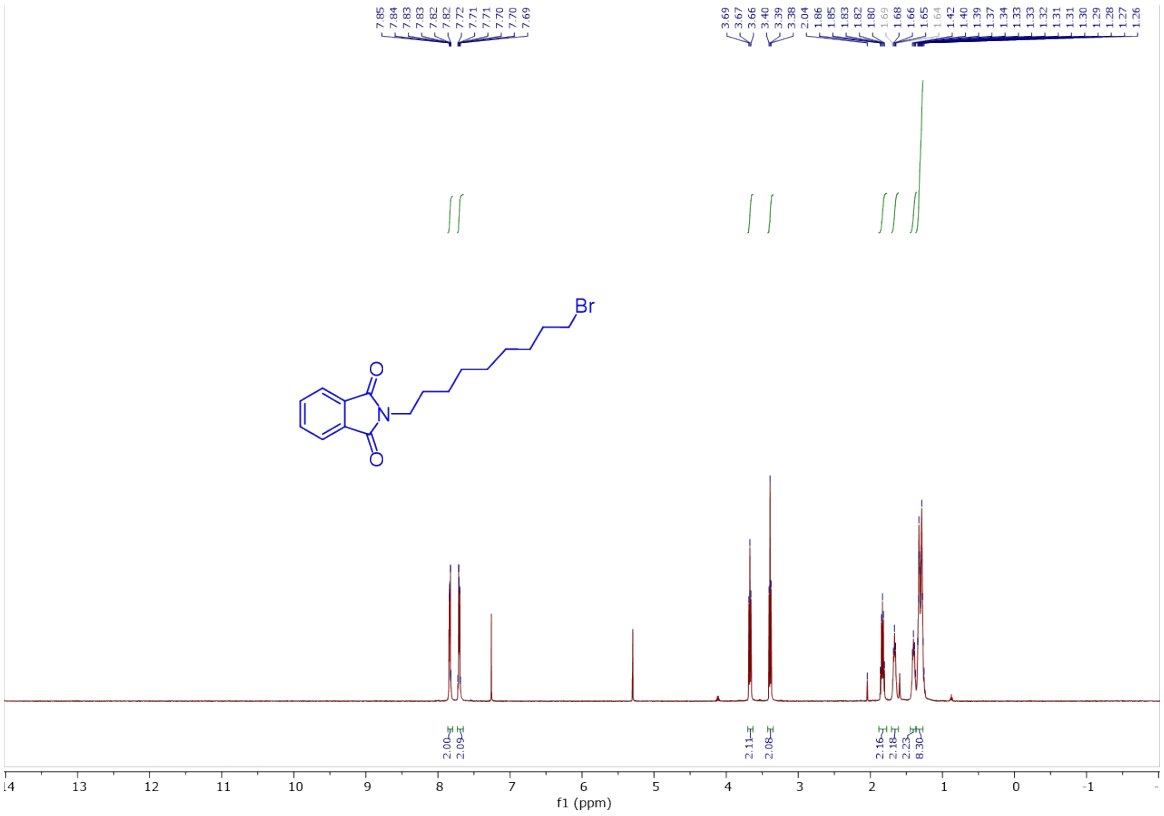
Br
f1 (ppm)

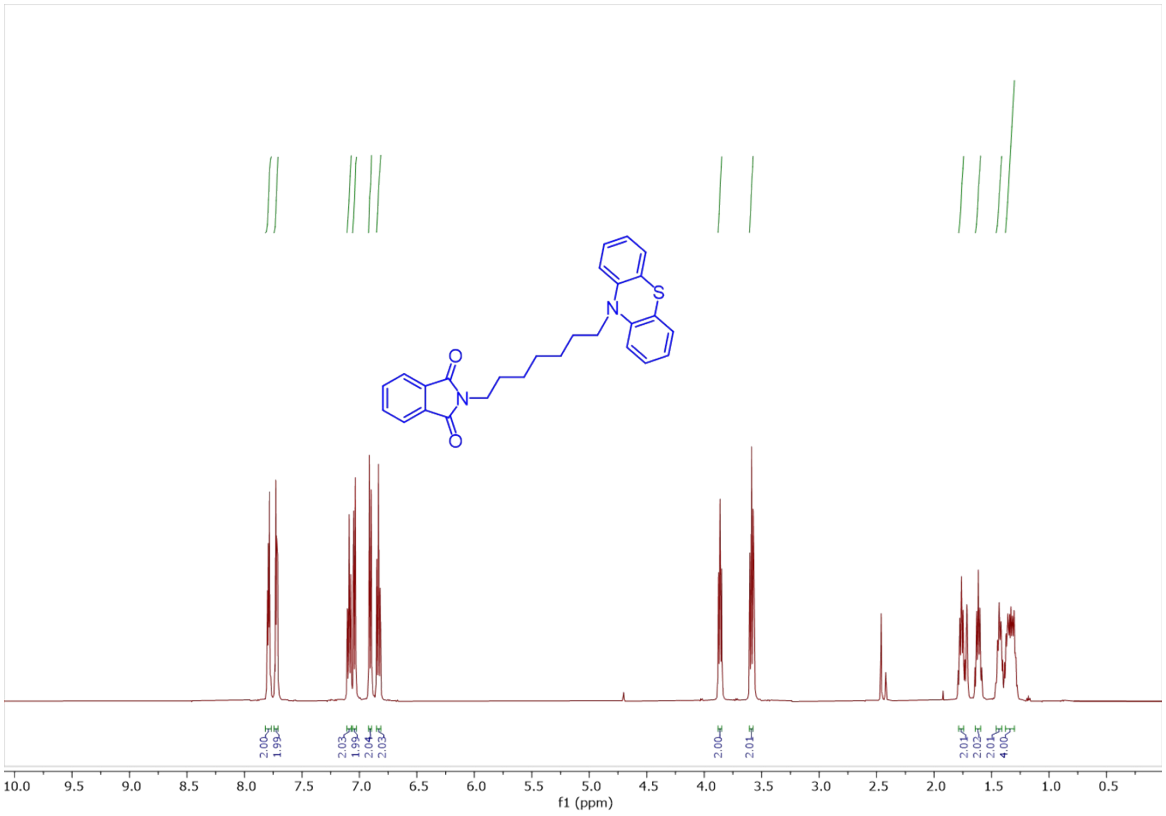
S
N
f1 (ppm)

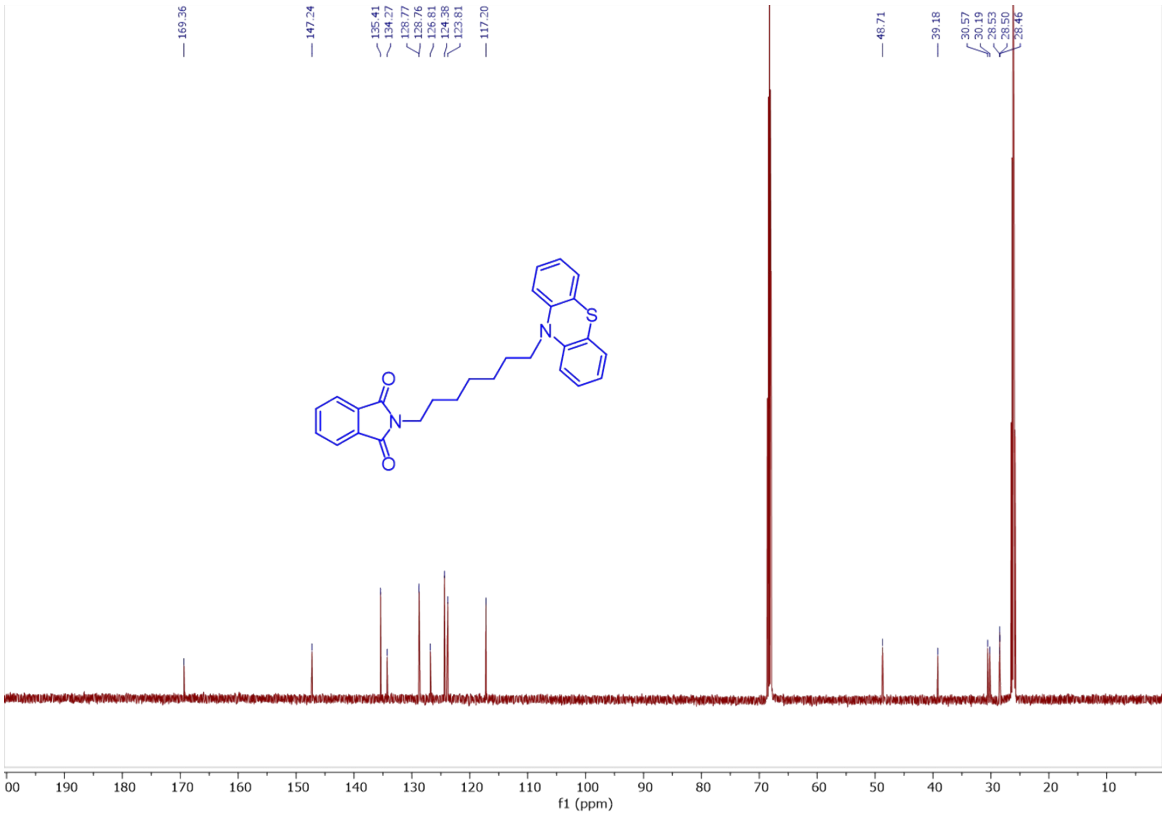
169.36
147.24
135.41
134.27
128.77
128.76
126.81
124.38
123.81
117.20
48.71
39.18
30.57
30.19
28.53
28.50
28.46
f1 (ppm)

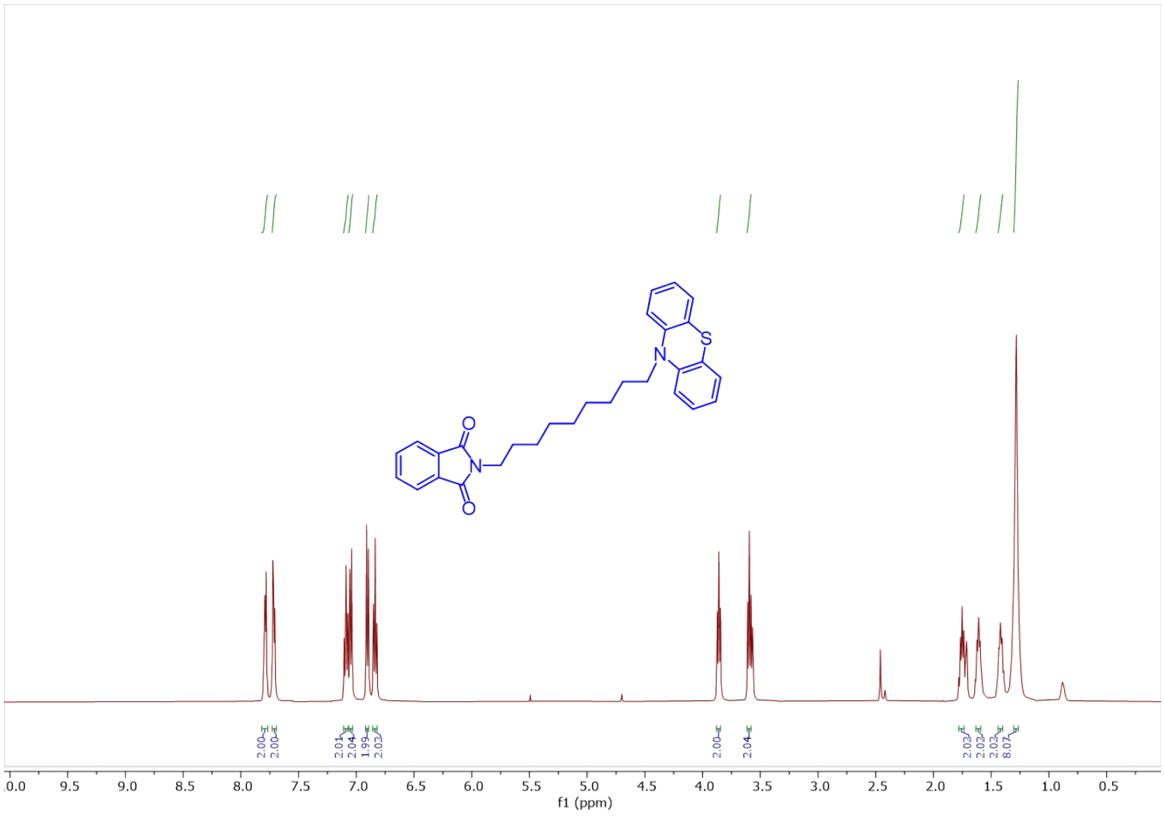
2.00
2.00
2.01
2.04
1.94
2.03
2.00
2.04
2.02
2.02
2.03
8.07
f1 (ppm)

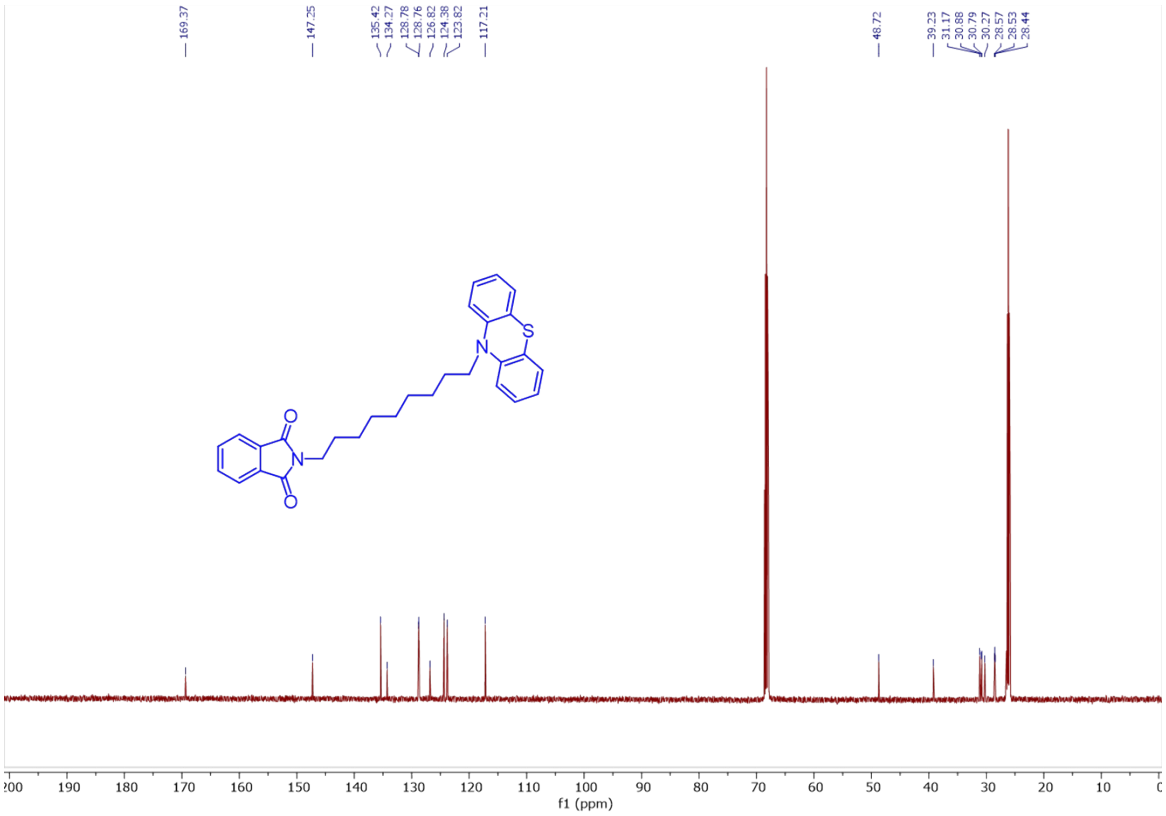

III. Supporting references.

1. Ghaem Maghami, M.; Dey, S.; Lenz, A. K.; Hobartner, C., Repurposing Antiviral Drugs for Orthogonal RNA-Catalyzed Labeling of RNA. *Angew Chem Int Ed* **2020,** *59* (24), 9335-9339.
2. Kohn, W.; Sham, L. J., Self-Consistent Equations Including Exchange and Correlation Effects. *Phys Rev* **1965,** *140* (4A), A1133-A1138.
3. Parr, R. G.; Yang, W., Density-functional theory of atoms and molecules. International Series of Monographs on Chemistry. *Oxford University Press, New York* **1994,** *3*, 14312-14321.
4. Frisch, M. J.; Trucks, G. W.; Schlegel, H. B.; Scuseria, G. E.; Robb, M. A.; Cheeseman, J. R.; Scalmani, G.; Barone, V.; Mennucci, B.; Petersson, G. A.; Nakatsuji, H.; Caricato, M.; Li, X.; Hratchian, H. P.; Izmaylov, A. F.; Bloino, J.; Zheng, G.; Sonnenberg, J. L.; Hada, M.; Ehara, M.; Toyota, K.; Fukuda, R.; Hasegawa, J.; Ishida, M.; Nakajima, T.; Honda, Y.; Kitao, O.; Nakai, H.; Vreven, T.; J. A. Montgomery, J.; Peralta, J. E.; Ogliaro, F.; Bearpark, M.; Heyd, J. J.; Brothers, E.; Kudin, K. N.; Staroverov, V. N.; Kobayashi, R.; Normand, J.; Raghavachari, K.; Rendell, A.; Burant, J. C.; Iyengar, S. S.; Tomasi, J.; Cossi, M.; Rega, N.; Millam, J. M.; Klene, M.; Knox, J. E.; Cross, J. B.; Bakken, V.; Adamo, C.; Jaramillo, J.; Gomperts, R.; Stratmann, R. E.; Yazyev, O.; Austin, A. J.; Cammi, R.; Pomelli, C.; Ochterski, J. W.; Martin, R. L.; Morokuma, K.; Zakrzewski, V. G.; Voth, G. A.; Salvador, P.; Dannenberg, J. J.; Dapprich, S.; Daniels, A. D.; Farkas, Ö.; Foresman, J. B.; Ortiz, J. V.; Cioslowski, J.; Fox, D. J. *Gaussian 09, Revision D.01*, Gaussian, Inc., Wallingford CT, 2009.
5. Rassolov, V. A.; Ratner, M. A.; Pople, J. A.; Redfern, P. C.; Curtiss, L. A., 6-31G*basis set for third-row atoms. *J Comput Chem* **2001,** *22* (9), 976-984.
6. Marenich, A. V.; Cramer, C. J.; Truhlar, D. G., Universal solvation model based on solute electron density and on a continuum model of the solvent defined by the bulk dielectric constant and atomic surface tensions. *J Phys Chem B* **2009,** *113* (18), 6378-96.

7. Agarwal, G.; Doan, H. A.; Assary, R. S., Molecular Structure and Electron Affinity of Metal-Solvent Complexes: Insights from Density Functional Theory Simulations. *J Electrochem Soc* **2020,** *167* (10), 100545.
8. Nicholson, R. S., Theory and Application of Cyclic Voltammetry for Measurement of Electrode Reaction Kinetics. *Anal Chem* **1965,** *37* (11), 1351-+.
9. Attanayake, N. H.; Kowalski, J. A.; Greco, K. V.; Casselman, M. D.; Milshtein, J. D.; Chapman, S. J.; Parkin, S. R.; Brushett, F. R.; Odom, S. A., Tailoring Two-Electron-Donating Phenothiazines To Enable High Concentration Redox Electrolytes for Use in Nonaqueous Redox Flow Batteries. *Chem Mater* **2019,** *31* (12), 4353-4363.
10. Zhang, C. K.; Niu, Z. H.; Ding, Y.; Zhang, L. Y.; Zhou, Y. G.; Guo, X. L.; Zhang, X. H.; Zhao, Y.; Yu, G. H., Highly Concentrated Phthalimide-Based Anolytes for Organic Redox Flow Batteries with Enhanced Reversibility. *Chem* **2018,** *4* (12), 2814-2825.
11. Armand, P.; Tillard, M.; Haidoux, A.; Daenens, L., Single-crystal growth, structure, and optical properties of a new non-centrosymmetric germanate, RbSbGe3O9. *J Solid State Chem* **2020,** *286*, 121290.
12. Krause, L.; Herbst-Irmer, R.; Sheldrick, G. M.; Stalke, D., Comparison of silver and molybdenum microfocus X-ray sources for single-crystal structure determination. *J Appl Crystallogr* **2015,** *48* (Pt 1), 3-10.
13. Sheldrick, G. M., SHELXT - Integrated space-group and crystal-structure determination. *Acta Cryst A* **2015,** *71* (1), 3-8.
14. Müller, P., Practical suggestions for better crystal structures. *Crystallogr Rev* **2009,** *15* (1), 57-83.
15. Hostaša, J.; Řezáča, J.; Hobzaa, P., On the performance of the semiempirical quantum mechanical PM6 and PM7 methods for noncovalent interactions. *Chem. Phys. Lett.* **2013,** *568-569*, 161-166.
16. Stewart, J. J. P. MOPAC2016.
17. Jorgensen, W. L.; Maxwell, D. S.; Tirado-Rives, J., Development and Testing of the OPLS All-Atom Force Field on Conformational Energetics and Properties of Organic Liquids. *J. Am. Chem. Soc.* **1996,** *118*, 11225–11236.
18. Kaminski, G. A.; Friesner, R. A.; Tirado-Rives, J.; Jorgensen, W. L., Evaluation and Reparametrization of the OPLS-AA Force Field for Proteins via Comparison with Accurate Quantum Chemical Calculations on Peptides. *J. Phys. Chem. B* **2001,** *105*, 6474-6487.
19. Dodda, L. S.; Vilseck, J. Z.; Tirado-Rives, J.; Jorgensen, W. L., 1.14*CM1A-LBCC: Localized Bond-Charge Corrected CM1A Charges for Condensed-Phase Simulations. *J. Phys. Chem. B* **2017,** *121*, 3864-3870.
20. Dodda, L. S.; Cabeza de Vaca, I.; Tirado-Rives, J.; Jorgensen, W. L., LigParGen web server: an automatic OPLS-AA parameter generator for organic ligands. *Nuclei Acid Res.* **2017,** *45*, W331-W336.
21. Breneman, C. M.; Wiberg, K. B., Determining atom-centered monopoles from molecular electrostatic potentials. The need for high sampling density in formamide conformational analysis. *J. Comput. Chem.* **1990,** *11*, 361-373.
22. Sigfridsson, E.; Ryde, U., Comparison of Methods for Deriving Atomic Charges from the Electrostatic Potential and Moments. *J. Comput. Chem.* **1997,** *19*, 377-395.
23. Martinez, L.; Andrade, R.; Birgin, E. G.; Martinez, J. M., Packmol: A Package for Building Initial Configurations for Molecular Dynamics Simulations. *J. Comput. Chem.* **2009,** *30*, 2157-2164.
24. van der Spoel, D.; Lindahl, E.; Hess, B.; G. Groenhof; Mark, A. E.; Berendsen, H. J. C., GROMACS: fast, flexible and free. *J. Comput. Chem.* **2005,** *26*, 1701-1718.
25. Humphrey, W.; Dalke, A.; Schulten, K., VMD - Visual Molecular Dynamics. **1996,** *14*, 33-38.
26. Csardi, G.; Nepusz, T., The igraph software package for complex network research. *InterJournal, Complex Systms* **2006,** *1695*, 1-9.
27. Yin, H.; Benson, A. R.; Leskovec, J., Higher-order clustering in networks. *Phys. Rev. E* **2018,** *97*, 052306.
28. Choi, J.-H.; Lee, H.; Choi, H. R.; Cho, M., Graph Theory and Ion and Molecular Aggregation in Aqueous Solutions. *Ann. Rev. Phys. Chem.* **2018,** *69*, 125-129.